Neutrino *CP* measurement in the presence of RG running with mismatched momentum transfers

Shao-Feng Ge,[1,2,*] Chui-Fan Kong,[1,2,†] and Pedro Pasquini[3,‡]

[1]*Tsung-Dao Lee Institute and School of Physics and Astronomy, Shanghai Jiao Tong University, Shanghai 200240, China*
[2]*Key Laboratory for Particle Astrophysics and Cosmology (MOE) and Shanghai Key Laboratory for Particle Physics and Cosmology, Shanghai Jiao Tong University, Shanghai 200240, China*
[3]*Department of Physics, University of Tokyo, Bunkyo-ku, Tokyo 113-0033, Japan*

The neutrino mixing parameters are expected to have renormalization group (RG) running effect in the presence of new physics. If the momentum transfers at production and detection mismatch with each other, the oscillation probabilities are generally modified and become dependent on not just the neutrino energy but also the momentum transfer. Even in the limit of vanishing baseline, the transition probability for the appearance channel is interestingly not zero. This would significantly affect the sensitivity of the genuine leptonic Dirac *CP* phase. We further explore the possibility of combining the long- and short-baseline neutrino experiments to constrain such RG running effect for the purpose of guaranteeing the *CP* measurement. To simulate the double dependence on the neutrino energy and momentum transfer, we extend the usual GLoBES simulation of fixed baseline experiments and use a two-dimensional χ^2 analysis to obtain sensitivities.

I. INTRODUCTION

The matter-antimatter asymmetry in the Universe is one of the most fundamental questions [1]. To explain this asymmetry, the charge-parity (*CP*) violation is necessary [2]. In the Standard Model (SM) of particle physics, the quark mixing matrix introduces a *CP* phase but the induced baryon asymmetry is too small to account for the observed value [3–5]. In the extended SM with heavy right-handed neutrinos, it has been shown that the leptonic *CP* violation could generate sufficient matter–antimatter disparity through the leptogenesis mechanism [6–8]. It is interesting to observe that the leptonic *CP* phases in the neutrino mixing matrix [9] provide potential sources of *CP* violation that can be directly used to explain the matter-antimatter asymmetry [10–16].

The leptonic Dirac *CP* phase δ_D of the Pontecorvo-Maki-Nakagawa-Sakata (PMNS) matrix can manifest itself in neutrino oscillation and hence can be measured therein. Its

*[*]gesf@sjtu.edu.cn
[†]kongcf@sjtu.edu.cn
[‡]pedrosimpas@g.ecc.u-tokyo.ac.jp

first measurement results were published in 2019 [17,18] by the two long-baseline (LBL) neutrino oscillation experiments NOνA [19] and T2K [20]. With the normal ordering (NO) of neutrino masses that is preferred by the latest results, the 2021 NOνA result gives $\delta_D = 148°^{+49°}_{-157°}$ [21] while the 2023 T2K result has $\delta_D = 247°^{+56°}_{-36°}$ [22]. The next-generation LBL experiments T2HK [23] and DUNE [24] under construction are expected to greatly improve the precision on δ_D. With about 10 years of data taking, each experiment can reach ∼10° precision level [25,26]. In addition, ESSνSB [27] is sensitive to δ_D by detecting neutrinos at the second oscillation peak, while T2HKK [28] and MOMENT [29] are sensitive to both the first and second oscillation maxima. With around twice the energy and baseline of DUNE, the P2O experiment [30] is sensitive to both δ_D and the matter effect. Additional low-energy neutrinos from muon decay at rest (μDAR) provide complementary measurements to accelerator LBL experiments, such as DAEδALUS [31], TNT2HK [32], μDARTS [33,34], DAEδALUS + JUNO [35], and DUNE + μTHEIA [36]. Besides accelerator neutrinos, *CP* measurement with sub-GeV atmospheric neutrino oscillation is also proposed for Super-PINGU [37,38], Super-ORCA [39], and even at JUNO [40] or DUNE [41].

Although the neutrino oscillation measurement has entered the precision era [42,43], the interpretation of the experimental data to extract the leptonic Dirac *CP* phase δ_D still faces various theoretical challenges. On the SM side, the matter density uncertainty can greatly reduce

the sensitivity to δ_D, especially when the value of δ_D is around the maximal values 90° or 270° [36,44–47]. Beyond the SM, there are various new physics scenarios that are capable of mimicking the CP violation effect and hence disturbing the CP measurement. For example, the neutrino nonstandard interaction (NSI) contributes extra matter potential [48,49] that receives different sign between neutrino and antineutrino modes to fake CP and significantly reduce the CP phase sensitivity [50–55]. In addition, the Lorentz invariance violation (LIV) [56,57] induces an effective Hamiltonian with both CPT-odd and CPT-even terms that have similar form as the effective Hamiltonian induced by NSI. Consequently, the effective Hamiltonian will modify the neutrino oscillation probability and hence impact on the CP phase sensitivity just like NSI [58–61]. Moreover, the nonunitary mixing due to heavy neutrinos [62,63] allows extra CP phases to fake the genuine CP effect [51,64–68].

Besides the new physics scenarios listed above, both the SM and the BSM interactions can generate less explored effects in neutrino oscillation such as the renormalization group (RG) running of the neutrino mixing parameters [69–74]. Various neutrino mass models, such as the canonical seesaw models, the inverse seesaw model, the scotogenic model, and the radiative Dirac model can lead to RG running effects [73,74]. Consequently, the neutrino mass and mixing parameters evolve as functions of the relevant energy scale. With mismatched energy scales between the neutrino production and detection processes, the neutrino RG running can affect its oscillation probabilities [75].

In our paper, we carefully study how RG running can affect the leptonic CP phase measurement. In Sec. II, we review the neutrino RG running features and introduce a model-independent parametrization for the running behaviors. We then establish in Sec. III the general formalism of neutrino oscillations in the presence of RG running. In particular, we adopt the quantum field theory (QFT) language and compare with the usually adopted quantum mechanics (QM) approach. With higher energy, DUNE can provide larger variation at the relevant energy scale than other experiments to allow more significant RG effects. In Sec. IV, we elaborate how a two-dimensional neutrino oscillation simulation, including neutrino energy and momentum transfer reconstructions, should be established for GLoBES with DUNE as a specific realization. The interplay between RG running and the genuine Dirac CP phase is evaluated with the extended two-dimensional χ^2 analysis to give the projected sensitivities at DUNE. Our conclusion and discussion about this new effect can be found in Sec. VI.

II. RG RUNNING OF NEUTRINO MIXING PARAMETERS

Although neutrino oscillation is the first new physics supported by various experimental measurements, we are still not so sure what is really happening behind the scene. The new physics that we have been looking for may not be as apparent as the nonstandard interactions (NSI) that appears at tree level already and affects the neutrino oscillation behavior, but make itself manifest via loop correction and the RG running effect. Studying the RG running effect in neutrino oscillation is actually an inevitable way of exploring new physics.

The neutrino mixing matrix U is defined according to the neutrino mass matrix diagonalization, $U^\dagger M_\nu^\dagger M_\nu U = \text{Diag}(m_1^2, m_2^2, m_3^2)$. In other words, the RG running effect of the neutrino mixing is inherited from the running of the neutrino mass matrix. On the model building side, the neutrino mass is typically generated at a high scale while the mass value and the corresponding neutrino mixing parameters are measured experimentally at a low scale. Across different energy scales, the RG evolution effects need to be included.

The RG running of neutrino mixing can be generally parametrized using the β function,

$$\frac{d\mathcal{O}_\nu}{d\ln|Q^2|} \equiv \beta_\nu, \qquad (2.1)$$

where $|Q^2|$ is the absolute value of momentum transfer [75]. Choosing the Lorentz-invariant momentum transfer $|Q^2|$ as the RG running variable is widely used in the literature and known as the Gell Mann-Low scheme [76,77]. Such a choice is consistent with the previous studies about the RG running effect in neutrino oscillations [75,78,79]. For generality, we use $\mathcal{O}_\nu$ to denote the neutrino observables such as the mixing angles and the Dirac CP phase. In neutrino oscillation, the neutrino propagates mainly as the on-shell mass eigenstates and the RG scale of the propagator is fixed as neutrino masses, $Q^2 = m_\nu^2$. Consequently, the RG running contribution from the neutrino propagator part can be ignored [75]. In other words, the RG running of the neutrino mixing matrix should come from the charged-current vertex part [75,78,79]. Both the neutrino production and the detection processes are affected by RG running via modification of the mixing angles and coupling constants with different scales. Below the new physics scale, the RG evolution determined by the SM [80,81] is negligibly small [74] and hence the mixing parameters are treated as constants. Any sizable RG running effect should appear above the new physics scale. The neutrino masses can also run in a similar way as Eq. (2.1). However, the impact of running neutrino masses is negligible [70–75] for the oscillation process of interest and hence omitted in this paper for simplicity.

For generality, we simply treat β_ν as a perturbative constant. In this sense, the solution of Eq. (2.1) for the three mixing angles ($\theta_s \equiv \theta_{12}$, $\theta_a \equiv \theta_{23}$, and $\theta_r \equiv \theta_{13}$) and the Dirac CP phase δ_D can be generally expressed as,
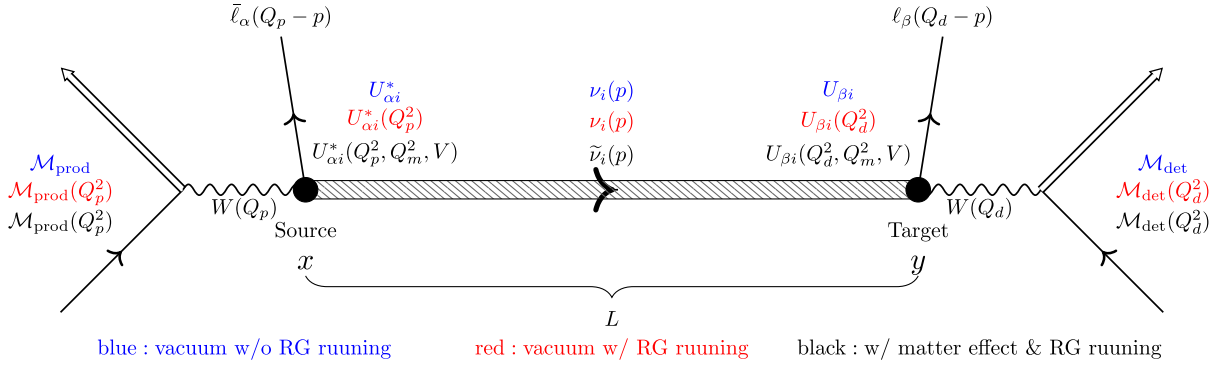
FIG. 1. The schematic plot for the QFT description of neutrino oscillation including three cases: (1) vacuum oscillation without considering RG running (blue); (2) vacuum oscillation with RG running (red); as well as (3) oscillation with both RG running and matter effect (black).

$$\theta_{ij}(Q^2) \equiv \theta_{ij}(Q_0^2) + \beta_{ij} \ln\left(\left|\frac{Q^2}{Q_0^2}\right|\right), \quad \text{and}$$

$$\delta_D(Q^2) \equiv \delta_D(Q_0^2) + \beta_\delta \ln\left(\left|\frac{Q^2}{Q_0^2}\right|\right). \tag{2.2}$$

The reference value $|Q_0^2|$ corresponds to the new physics scale and the evolution formulas apply for $|Q^2| > |Q_0^2|$ while reducing to constant values for $|Q^2| < |Q_0^2|$. If the new physics scale is much higher than the experimental scales, the running effect will not be measured at the current low energy neutrino experiments. To test the running effect at the $\mathcal{O}(\text{GeV})$ LBL experiments such as DUNE, we take $Q_0^2 = 1$ MeV as a benchmark value throughout this paper. Furthermore, we need four parameters to describe the evolution, three β_{ij} for the mixing angles and one β_δ for the Dirac *CP* phase. The RG running effect can lead to nonstandard oscillation behaviors as we elaborate below.

III. GENERAL FORMALISM OF NEUTRINO OSCILLATION

A. QFT description of neutrino oscillation

We start with the vacuum neutrino oscillation without considering RG running which is conceptually clearer to set the stage in the QFT framework. A typical neutrino oscillation experiment involves the neutrino production, propagation, and detection processes. For the case of neutrino (rather than antineutrino) oscillation, a charged antilepton $\overline{\ell}_\alpha$ appears at the position $x \equiv (x_0, \boldsymbol{x})$ when producing an α-flavor neutrino ν_α while a charged lepton ℓ_β is observed at the position $y \equiv (y_0, \boldsymbol{y})$ for the detection of a β-flavor neutrino ν_β as shown in Fig. 1. In between, neutrinos propagate as mass eigenfields ($\nu_i \equiv \sum_\alpha U_{\alpha i}^* \nu_\alpha$) over a macroscopic spatial distance $\boldsymbol{L} \equiv \boldsymbol{y} - \boldsymbol{x}$. The full transition matrix element $\mathcal{T}$ for the above processes can be read off directly from Fig. 1 [82],

$$\mathcal{T} \equiv \sum_i \int d^4x\, d^4y\, \mathcal{M}_{\text{det}}^\mu(y) \frac{ig}{\sqrt{2}} U_{\beta i} \bar{u}_\beta \gamma_\mu P_L \int \frac{d^4p}{(2\pi)^4} \frac{i(\not{p} + m_i)e^{ip\cdot(x-y)}}{p^2 - m_i^2 + i\epsilon} \frac{ig}{\sqrt{2}} U_{\alpha i}^* \gamma_\nu P_L v_\alpha \mathcal{M}_{\text{prod}}^\nu(x), \tag{3.1}$$

where the production and detection matrix elements $\mathcal{M}_{\text{prod}}^\mu(x)$ and $\mathcal{M}_{\text{det}}^\mu(y)$ contain those relevant interactions except the charged-current vertex between neutrino and charged lepton. To also take the associated charged leptons into consideration, the charged current (CC) interaction mediated by the SM $W^\pm$ boson with weak gauge coupling g should be involved. With $\bar{\psi}$ to produce a neutrino, the associated matrix element $U_{\alpha i}^*$ receives a complex conjugation. Similarly, the detection part annihilates the intermediate neutrino with ψ to have $U_{\beta i}$. The projector P_L selects the left-handed fermions.

The oscillation behavior as a periodic function of the baseline L is encoded in the propagation phase factor $e^{ip\cdot(x-y)}$ from x to y. For the mass eigenstate ν_i propagator,

$$\int \frac{d^4p}{(2\pi)^4} \frac{i(\not{p} + m_i)e^{ip\cdot(x-y)}}{p^2 - m_i^2 + i\epsilon} = \int \frac{d^4p}{(2\pi)^4} \frac{i\sum_s u_i(p,s)\bar{u}_i(p,s)e^{ip\cdot(x-y)}}{p^2 - m_i^2 + i\epsilon}, \tag{3.2}$$

its numerator can be replaced by two neutrino spinors according to the spin sum relation, $\not{p} + m_i = \sum_s u_i(p,s)\bar{u}_i(p,s)$. In the ultrarelativistic limit, only the left-handed chiral component can contribute since the right-handed counterpart is projected out by $P_L u(p,+) = 0$. Then the neutrino spinors $u_i(p,-)\bar{u}_i(p,-)$ in the numerator complete the matrix elements for production and detection,

$$\mathcal{M}_{\text{prod}}(x) \equiv \frac{ig}{\sqrt{2}}\bar{u}_i(p,-)\gamma_\nu P_L v_\alpha \mathcal{M}^\nu_{\text{prod}}(x), \qquad (3.3a)$$

$$\mathcal{M}_{\text{det}}(y) \equiv \frac{ig}{\sqrt{2}}\mathcal{M}^\mu_{\text{det}}(y)\bar{u}_\beta\gamma_\mu P_L u_i(p,-). \qquad (3.3b)$$

Since the neutrino mass is typically much smaller than the momentum transfer in production and detection, their matrix elements $\mathcal{M}_{\text{prod}}$ and $\mathcal{M}_{\text{det}}$ are essentially independent of the neutrino masses. Consequently, the sum over the mass eigenstantes involves only the neutrino propagator,

$$\mathcal{T} = \int \frac{d^4 p}{(2\pi)^4} d^4 x d^4 y \mathcal{M}_{\text{det}}(y)$$
$$\times \left[\sum_i U_{\beta i}\frac{ie^{ip\cdot(x-y)}}{p^2 - m_i^2 + i\epsilon}U^*_{\alpha i}\right]\mathcal{M}_{\text{prod}}(x). \qquad (3.4)$$

The integral over the four-momentum p is divided into two parts, the integration over the three momentum $\boldsymbol{p}$ and energy p_0, respectively. The three-momentum integration can be calculated using the Grimus-Stockinger theorem [82],

$$\int \frac{d^3\boldsymbol{p}}{(2\pi)^3} f(\boldsymbol{p})\frac{e^{ip\cdot L}}{p_0^2 - \boldsymbol{p}^2 - m_i^2 + i\epsilon}$$
$$\xrightarrow{|L|\to\infty} -\frac{1}{4\pi L} f(|\boldsymbol{p}|\hat{\boldsymbol{L}})e^{i|\boldsymbol{p}|L}\Big|_{|\boldsymbol{p}|=\sqrt{p_0^2 - m_i^2}}, \qquad (3.5)$$

with the exponential term being $e^{-ip\cdot(x-y)} = e^{ip\cdot L}$. The above equation means that the leading contribution is given by neutrinos on mass shell, $|\boldsymbol{p}| \approx p_0 - m_i^2/2p_0$, and propagating from source to detector in the direction of $\hat{\boldsymbol{L}} = \boldsymbol{L}/|\boldsymbol{L}|$. Most importantly, the full transition matrix element,

$$\mathcal{T} \propto \frac{1}{L}\int dp_0 d^4 x d^4 y \mathcal{M}_{\text{det}}(y)\left(\sum_i U_{\beta i}e^{-i\frac{m_i^2}{2p_0}L}U^*_{\alpha i}\right)\mathcal{M}_{\text{prod}}(x), \qquad (3.6)$$

is inversely proportional to the baseline L which becomes a flux dilution factor $1/L^2$ in $|\mathcal{T}|^2$ due to neutrino number conservation in the three-dimensional space. The two spatial and one energy p_0 integrations result in a δ—function for energy conservation of the whole process [82]

with explicit calculation and more details to be found in [82–85]. For macroscopic distance, the total process decomposes into the neutrino flux from production, the neutrino scattering cross section of detection, and the neutrino oscillation probability.

The neutrino oscillation probability, $P_{\nu_\alpha \to \nu_\beta}$, is then defined as the absolute value squared of the amplitude in Eq. (3.6),

$$P_{\alpha\beta} \equiv |\mathcal{A}^{\text{osc}}_{\beta\alpha}|^2, \quad \text{with} \quad \mathcal{A}^{\text{osc}}_{\beta\alpha} \equiv \sum_i U_{\beta i}e^{-i\frac{m_i^2}{2E_\nu}L}U^*_{\alpha i}, \qquad (3.7)$$

by extracting those irrelevant terms for the oscillation probability to reduce to a δ function, $P_{\alpha\beta}(L=0) = \delta_{\alpha\beta}$. We can see that the amplitude $\mathcal{A}^{\text{osc}}_{\beta\alpha}$ is exactly the parenthesis of Eq. (3.6).

Note that the above QFT formalism for neutrino oscillation has two major differences with its quantum mechanics (QM) counterpart. In QM, the α flavor neutrino ν_α is described by a quantum state $|\nu_\alpha\rangle \equiv a_\alpha^\dagger|0\rangle$ and similarly for the mass eigenstate $|\nu_i\rangle \equiv a_i^\dagger|0\rangle$. Since $\nu_\alpha \equiv \sum_i U_{\alpha i}\nu_i$, the neutrino operators a_α and a_i (not b_α or b_i) have the same similarity transformation $a_\alpha = \sum_i U_{\alpha i}a_i$ according to $\nu \sim a + b^\dagger$. Then, the similarity transformation on the quantum states, $|\nu_\alpha\rangle = \sum_i U^*_{\alpha i}|\nu_i\rangle$, receives an extra complex conjugation. The second difference appears in the oscillation phase factor, $e^{-iE_i t}$, which has a minus sign according to the Schrodinger equation while its counterpart from the neutrino propagator in QFT is $e^{i|\boldsymbol{p}|L}$ without minus sign. With simultaneous presence of both differences, the oscillation probability derived in both QFT and QM formalism is the same.

B. Vacuum oscillation with RG running and zero-distance effect

Note that physical variables such as the neutrino mixing parameters and masses depend on momentum transfer in the presence of RG running as mentioned in Sec. II. Especially for a typical neutrino oscillation experiment, the momentum transfers in neutrino production, propagation, and detection processes are different from each other. However, since the neutrino mass receives negligible RG running effect [70–75], the neutrino mass eigenfields can be treated universally during the whole process. In this sense, the neutrino flavor eigenfields become momentum transfer dependent via the mixing matrix $U(Q^2)$, $\nu_\alpha(Q^2) \equiv \sum_i U_{\alpha i}(Q^2)\nu_i$. Besides the neutrino mixing matrices and neutrino flavor eigenfields, quantum corrections can also generate a RG running effect on the gauge coupling g of CC weak interactions, $g \to g(Q^2)$ [75]. As shown in Fig. 1, the full transition matrix element for the vacuum oscillation with RG running effect can be obtained by replacing the relevant parameters in Eq. (3.6) with their Q^2-dependent counterparts,

$$\mathcal{T} = -\frac{i}{8\pi^2 L} \int dp_0 d^4 x d^4 y \mathcal{M}_{\text{det}}(y, Q_d^2)$$

$$\times \left[\sum_i U_{\beta i}(Q_d^2) e^{-i\frac{m_i^2}{2E_\nu}L} U_{\alpha i}^*(Q_p^2) \right] \mathcal{M}_{\text{prod}}(x, Q_p^2), \quad (3.8)$$

where the momentum transfers in the neutrino production and detection processes are defined as Q_p^2 and Q_d^2. Finally, the vacuum oscillation amplitude with the RG running effect receives a modification on the mixing matrix from Eq. (3.7),

$$\mathcal{A}_{\beta\alpha}^{\text{osc}} = U_{\beta i}(Q_d^2) e^{-iL\frac{m_i^2}{2E_\nu}} U_{\alpha i}^*(Q_p^2). \quad (3.9)$$

The oscillation amplitude and consequently the corresponding probability $P_{\alpha\beta}(E_\nu, Q_p^2, Q_d^2)$ have dependence on the production and detection momentum transfers in addition to the neutrino energy.

The matrix elements $\mathcal{M}_{\text{prod}}(x, Q_p^2)$ and $\mathcal{M}_{\text{det}}(y, Q_d^2)$ absorb the Q^2-dependent gauge couplings $g(Q_p^2)$ and $g(Q_d^2)$, respectively. For simplicity, we focus on the running effect that enters the oscillation probability to emphasize its effect on the oscillation behaviors. However, the gauge coupling can also enter the oscillation probability through the matter effect as we elaborate later in Sec. III C.

From Eq. (3.9), an interesting effect emerges. The transition probability does not vanish in the zero-distance limit,

$$P_{\alpha\beta} = |[U(Q_d^2)U^\dagger(Q_p^2)]_{\beta\alpha}|^2, \quad (3.10)$$

if the mixing matrices $U(Q_p^2)$ and $U(Q_d^2)$ in the production and detection processes mismatch with each other. On the other hand, the oscillation probability $P_{\alpha\beta}$ reduces to $\delta_{\alpha\beta}$ if $Q_d^2 = Q_p^2$. Notice that zero-distance represents the distance of a short-baseline experiment with $L \ll 2E_\nu / \Delta m_{ij}^2$. At the same time, the condition $|L| \to \infty$ in Eq. (3.5) is still true as long as $LE_\nu \gg 1$ [82]. In other words, the so-called zero-distance is macroscopic and the neutrinos are on-shell, which means the production and detection processes are still separated. One should keep in mind that this is just a limit and not really zero distance. Therefore, the Grimus-Stockinger theorem can still be used in the zero-distance limit since the condition $1/E_\nu \ll L \ll 2E_\nu/\Delta m_{ij}^2$ is valid for all the short-baseline neutrino experiments we consider later.

The zero-distance transition probability can be explicitly calculated by using the standard PMNS parametrization [9],

$$U_{\text{PMNS}} \equiv O_{23} P_{\delta_D}^* O_{13} P_{\delta_D} O_{12}, \quad (3.11)$$

where O_{ij} are the Euler rotation matrices and $P_{\delta_D} \equiv \text{diag}\{1, 1, e^{-i\delta_D}\}$. Since we mainly focus on the RG running of the Dirac *CP* phase δ_D, we simply fix the other oscillation parameters except the *CP* phase and define the change of δ_D due to RG running as $\Delta\delta_D(Q_{d,p}^2) \equiv \delta_D(Q_d^2) - \delta_D(Q_p^2)$, where $\delta_{p,d} \equiv \delta_D(Q_{p,d}^2)$ represent the running *CP* phases in production and detection, respectively. Then the transition amplitude $U(Q_d^2)U^\dagger(Q_p^2)$ becomes,

$$\mathbb{1} + \frac{e^{-i\Delta\delta_D} - 1}{2} \begin{pmatrix} 2\sin^2\theta_r & e^{-i\delta_p} s_a \sin 2\theta_r & e^{-i\delta_p} c_a \sin 2\theta_r \\ e^{i\delta_d} s_a \sin 2\theta_r & -2e^{i\Delta\delta_D} s_a^2 \sin^2\theta_r & -2e^{i\Delta\delta_D} s_a c_a \sin^2\theta_r \\ e^{i\delta_d} c_a \sin 2\theta_r & -2e^{i\Delta\delta_D} s_a c_a \sin^2\theta_r & -2e^{i\Delta\delta_D} c_a^2 \sin^2\theta_r \end{pmatrix}. \quad (3.12)$$

It is interesting to see that it contains only the reactor (θ_r) and atmospheric (θ_a) mixing angles while the solar angle (θ_s) does not appear at all. Then the explicit form of the zero-distance transition probability is obtained by putting the above expression into Eq. (3.10). For $\nu_e \to \nu_e$ and $\nu_\mu \to \nu_e$, the transition probabilities are,

$$P_{ee}(Q_{d,p}^2) = 1 - \sin^2\left(\frac{\Delta\delta_D}{2}\right)\sin^2 2\theta_{13},$$

$$P_{\mu e}(Q_{d,p}^2) = \sin^2\left(\frac{\Delta\delta_D}{2}\right) s_{23}^2 \sin^2 2\theta_{13}. \quad (3.13)$$

Although these probabilities are independent of the Dirac *CP* phase itself, but are functions of the *CP* phase difference induced by the running effect. Most interestingly, the P_{ee} oscillation probability that is typically independent of

the Dirac *CP* phase has dependence on the *CP* phase difference induced by the RG running parameter $\Delta\delta_D$. The zero-distance effect is unique for identifying the running effect. On the experimental side, such an effect can be constrained using the data from the short-baseline (SBL) experiments as elaborated later in Sec. V.

C. Neutrino oscillation in matter with RG running

The neutrinos propagating in matter can experience that matter effect that arises from the forward scattering mediated by weak gauge bosons. It adds an additional matter potential matrix V to the vacuum Hamiltonian H_0,

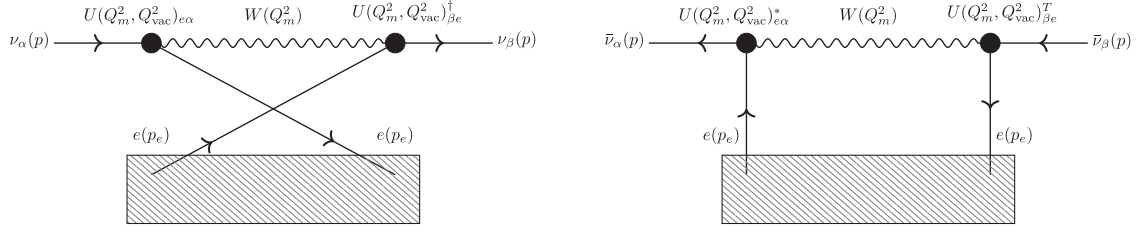$$H \equiv H_0 + V. \quad (3.14)$$

FIG. 2. The Feynman diagrams for the neutrino (left) and antineutrino (right) matter effects.

Note that the vacuum Hamiltonian $H_0 \equiv M^\dagger M / 2E_\nu$ is usually defined in the vacuum flavor basis $\nu_\alpha(Q^2_{\rm vac})$ where the momentum transfer is denoted as $Q^2_{\rm vac}$. Although there is no unique definition of $Q^2_{\rm vac}$ and its value is unknown, the introduction of this momentum transfer scale will not bring any problems since it will not appear in the final expression of oscillation probability as we show below. To ensure that the summation between H_0 and the matter potential matrix V makes sense, the latter needs to be written in the same flavor basis as H_0.

Recall that the neutrino flavor eigenfields depend on the momentum transfer. Similarly the matter flavor basis is defined at the momentum transfer Q^2_m of neutrino-matter interactions. As specifically shown in Fig. 2, the neutrino and antineutrino matter interactions are contributed by different Feynman diagrams. Although both arise from the W boson mediation, their momentum transfers are different,

$$\nu: Q^2_m \equiv |(p_\nu - p_e)^2| = |m^2_e - 2m_e E_\nu|,$$
$$\bar{\nu}: Q^2_m \equiv |(p_\nu + p_e)^2| = |m^2_e + 2m_e E_\nu|, \qquad (3.15)$$

which should not be a vanishing value as adopted in [75]. Between the neutrino and antineutrino modes, the momentum transfer $Q^2_m = |m^2_e \mp 2m_e E_\nu|$ differs. Consequently, the matter flavor eigenfields with Q^2_m dependence are no longer the same as their vacuum counterparts and the usual definition of the matter potential without considering RG running no longer holds.

The matter potential matrix should be diagonal in the matter flavor basis $\nu_\alpha(Q^2_m)$,

$$V \equiv \begin{pmatrix} \sqrt{2}G_F n_e & 0 & 0 \\ 0 & 0 & 0 \\ 0 & 0 & 0 \end{pmatrix}. \qquad (3.16)$$

To match with the vacuum Hamiltonian H_0, the matter potential matrix needs to be rotated to the vacuum flavor basis $\nu_\alpha(Q^2_{\rm vac})$. The connection between the vacuum $[\nu_\alpha(Q^2_{\rm vac})]$ and matter $[\nu_\alpha(Q^2_m)]$ flavor eigenfields is established through the commonly shared mass eigenfields ν_i, $\nu_\alpha(Q^2) = \sum_i U_{\alpha i}(Q^2)\nu_i$,

$$\nu_\alpha(Q^2_m) = \sum_i U_{\alpha i}(Q^2_m)\nu_i$$
$$= \sum_{i\beta} U_{\alpha i}(Q^2_m)U^*_{\beta i}(Q^2_{\rm vac})\nu_\beta(Q^2_{\rm vac}). \qquad (3.17)$$

For convenience, we define $U(Q^2_m, Q^2_{\rm vac}) \equiv U(Q^2_m)U^\dagger(Q^2_{\rm vac})$. Although the production, detection, and even the matter interaction processes involve different momentum transfers and hence should have different flavor eigenfields, the vacuum mass eigenfields is always defined for on-shell neutrinos. This property is based on the observation that the neutrino mass receives a very tiny RG running effect [70–75]. Now the total Hamiltonian can be written in the common vacuum flavor eigenfields $[\nu_\alpha(Q^2_{\rm vac})]$ using the transformation between vacuum and matter flavor eigenfields in Eq. (3.17), $H = M^\dagger M / 2E_\nu + U^\dagger(Q^2_m, Q^2_{\rm vac})VU(Q^2_m, Q^2_{\rm vac})$. After a similarity transformation $H \to U^\dagger(Q^2_{\rm vac})HU(Q^2_{\rm vac})$, the total Hamiltonian can be written in the vacuum mass eigenfields,

$$H = \frac{M^2_d}{2E_\nu} + U^\dagger(Q^2_m)VU(Q^2_m), \qquad (3.18)$$

where $M^2_d \equiv U^\dagger(Q^2_{\rm vac})M^\dagger M U(Q^2_{\rm vac}) \equiv {\rm diag}\{m^2_1, m^2_2, m^2_3\}$ is the diagonal mass matrix in vacuum. The undetermined $Q^2_{\rm vac}$ does not appear in this Hamiltonian anymore and will not affect the oscillation probability.

The diagonalization of the total Hamiltonian will give the effective mass eigenfields $\tilde{\nu}_i$ with the effective masses $\tilde{m}_i$ during the propagation by one unitary matrix $U(Q^2_m, V)$,

$$H_d \equiv U^\dagger(Q^2_m, V)HU(Q^2_m, V) \equiv {\rm diag}\left\{\frac{\tilde{m}^2_1}{2E_\nu}, \frac{\tilde{m}^2_2}{2E_\nu}, \frac{\tilde{m}^2_3}{2E_\nu}\right\}. \qquad (3.19)$$

The vacuum mass eigenfields ν_i and the effective mass eigenfields $\tilde{\nu}_i$ in matter are connected via the same unitary matrix $U(Q^2_m, V)$, $\nu_i = \sum_j U_{ij}(Q^2_m, V)\tilde{\nu}_j(Q^2_m, V)$. It can reduce to $\nu_i = \tilde{\nu}_i$ in the absence of matter potential V as expected. Note that the matrix $U(Q^2_m, V)$ is only used to diagonalize the total Hamiltonian.

To connect propagation with the production and detection processes, the relation between the effective mass

eigenfields $\tilde{\nu}_i$ in matter and the production as well as detection flavor eigenfields $\nu_\alpha(Q_{p,d}^2)$ is needed. Since the production and detection flavor eigenfields connect with the vacuum mass eigenfields ν_j via $\nu_\alpha(Q_{p,d}^2) = \sum_i U_{\alpha i}(Q_{p,d}^2)\nu_i$, the effective mass eigenfields correlate with the production and detection flavor eigenfields,

$$\nu_\alpha(Q_{p,d}^2) = \sum_{ij} U_{\alpha i}(Q_{p,d}^2)U_{ij}(Q_m^2, V)\tilde{\nu}_j(Q_m^2, V)$$

$$\equiv \sum_\alpha U_{\alpha j}(Q_{p,d}^2, Q_m^2, V)\tilde{\nu}_j(Q_m^2, V), \qquad (3.20)$$

where we define a unitary matrix $U(Q_{p,d}^2, Q_m^2, V) \equiv U(Q_{p,d}^2)U(Q_m^2, V)$ for convenience.

Now the oscillation formula for the vacuum case in Sec. III B can easily extend to the matter case. Reviewing the whole oscillation process shown in Fig. 1, the neutrino is first produced with flavor α, which decomposes into effective neutrino mass eigenfields with an associated matrix $U_{\alpha i}^*(Q_p^2, Q_m^2, V)$. After propagating a macroscopic spatial distance L, each effective mass eigenfield with the effective mass $\tilde{m}_i$ receives a phase factor, $e^{-iL\frac{\tilde{m}_i^2}{2E_\nu}}$. Finally, the effective mass eigenfields combine linearly with coefficients $U_{\beta i}(Q_d^2, Q_m^2, V)$ to flavor eigenfields $\nu_\beta(Q_d^2)$ to be detected. Then the net effect gives the oscillation amplitude,

$$\mathcal{A}_{\beta\alpha}^{\mathrm{osc}} \equiv \sum_i U_{\beta i}(Q_d^2, Q_m^2, V)e^{-iL\frac{\tilde{m}_i^2}{2E_\nu}}U_{i\alpha}^\dagger(Q_p^2, Q_m^2, V). \quad (3.21)$$

The above amplitude reduces to the vacuum one when the matter potential is vanishing with $U(Q_{p,d}^2, Q_m^2, V) \to U(Q_{p,d}^2)$ and $\tilde{m}_i \to m_i$ as expected. Different from the vacuum case, the oscillation amplitude with matter effect involves one more momentum transfer Q_m^2 which is not negligible when considering the RG running effect. Besides, the gauge coupling enters the oscillation amplitude/probability through the matter potential term of the total Hamiltonian as shown in Eq. (3.18). For simplicity, we do not consider the RG running effect on the coupling constant but only the mixing parameters in this paper.

D. Numerical illustration of the RG running effect

To illustrate the RG running effect on the neutrino oscillation probabilities (dashed, dotted, and dash-dotted curves), we compare with the standard result (solid curves) in Fig. 3. For all panels, we take the DUNE configuration with $L = 1284.9$ km, $E_\nu \in [0.5\ \mathrm{GeV}, 5\ \mathrm{GeV}]$, and production momentum transfer $Q_p^2 = (p_{\nu_\mu} + p_\mu)^2 = m_\pi^2$ for neutrinos produced from pion decay. However, the detection momentum transfer Q_d^2 depends on the interaction with the target and its value can vary a lot as we show below in

Sec. IV A. The upper left/right panel shows the RG running effect on the $\nu_\mu \to \nu_e/\bar{\nu}_\mu \to \bar{\nu}_e$ oscillation probabilities with three β_δ [defined in Eq. (2.2)] values: $\beta_\delta = 0$ (without RG running), -3×10^{-2}, and 3×10^{-2}. For both panels, there are three oscillation peaks which locate at $E_\nu \sim 0.5$, 0.8, 2.5 GeV, respectively. Among these three oscillation peaks, the 2.5 GeV one contributes most to the event rate at DUNE since the DUNE neutrino spectrum peaks in this region. For neutrino energies within [2 GeV, 3 GeV], the relative oscillation probability difference $[\equiv |P(\beta_\delta \neq 0) - P(\beta_\delta = 0)|/P(\beta_\delta = 0)]$ can reach percentage level and has a similar size as the *CP* effect. Hence the RG running effect on neutrino oscillation probabilities is not negligible.

In the lower panels of Fig. 3, we study the impact on oscillation probabilities with three different Q_d^2 values: $Q_d^2 = 0.1\ \mathrm{GeV}^2$, $1\ \mathrm{GeV}^2$, and $8\ \mathrm{GeV}^2$. For the neutrino mode, the numerical result shows that the three blue curves with different Q_d^2 values are close to each other for E_ν below 2.5 GeV and can be distinguished for E_ν above 2.5 GeV. However, for the antineutrino mode, these curves are distinguishable for E_ν from 2 GeV up to 5 GeV. Hence for a real neutrino experiment like DUNE, the momentum transfer should be carefully reconstructed in order to study the RG running effect as we elaborate below.

IV. *CP* PHASE SENSITIVITY REDUCTION AT DUNE

A major concern is that the neutrino *CP* measurement will suffer from the RG running effect. As mentioned above, the oscillation probability with RG running can vary a lot with the neutrino energy E_ν and the detection momentum transfer Q_d^2. Such effect appears when the two momentum transfers in neutrino production (Q_p^2) and detection (Q_d^2) mismatch. The larger mismatch the larger RG running effect. With large neutrino energy, DUNE can provide a large detection momentum transfer and hence a large RG running effect. So we take DUNE as an example to quantitatively study the impact.

A. Neutrino energy and momentum transfer reconstructions

The production momentum transfer has a fixed value as the pion mass $Q_p^2 = m_\pi^2$ since most DUNE neutrinos are generated through pion decay [86]. To evaluate the oscillation probability $P_{\alpha\beta}(E_\nu, Q_p^2, Q_d^2)$ with the RG running effect, one still needs to reconstruct the neutrino energy E_ν and the detection momentum transfer Q_d^2. The neutrino energy, $E_\nu^{\mathrm{rec}} \equiv E_\ell^{\mathrm{rec}} + E_{\mathrm{had}}^{\mathrm{rec}}$, is reconstructed from the deposited lepton (E_ℓ^{rec}) and hadronic ($E_{\mathrm{had}}^{\mathrm{rec}}$) energies [24]. On the other hand, the reconstructed detection momentum transfer Q_{rec}^2 correlates to not just the reconstructed neutrino energy E_ν^{rec}, but also the measured
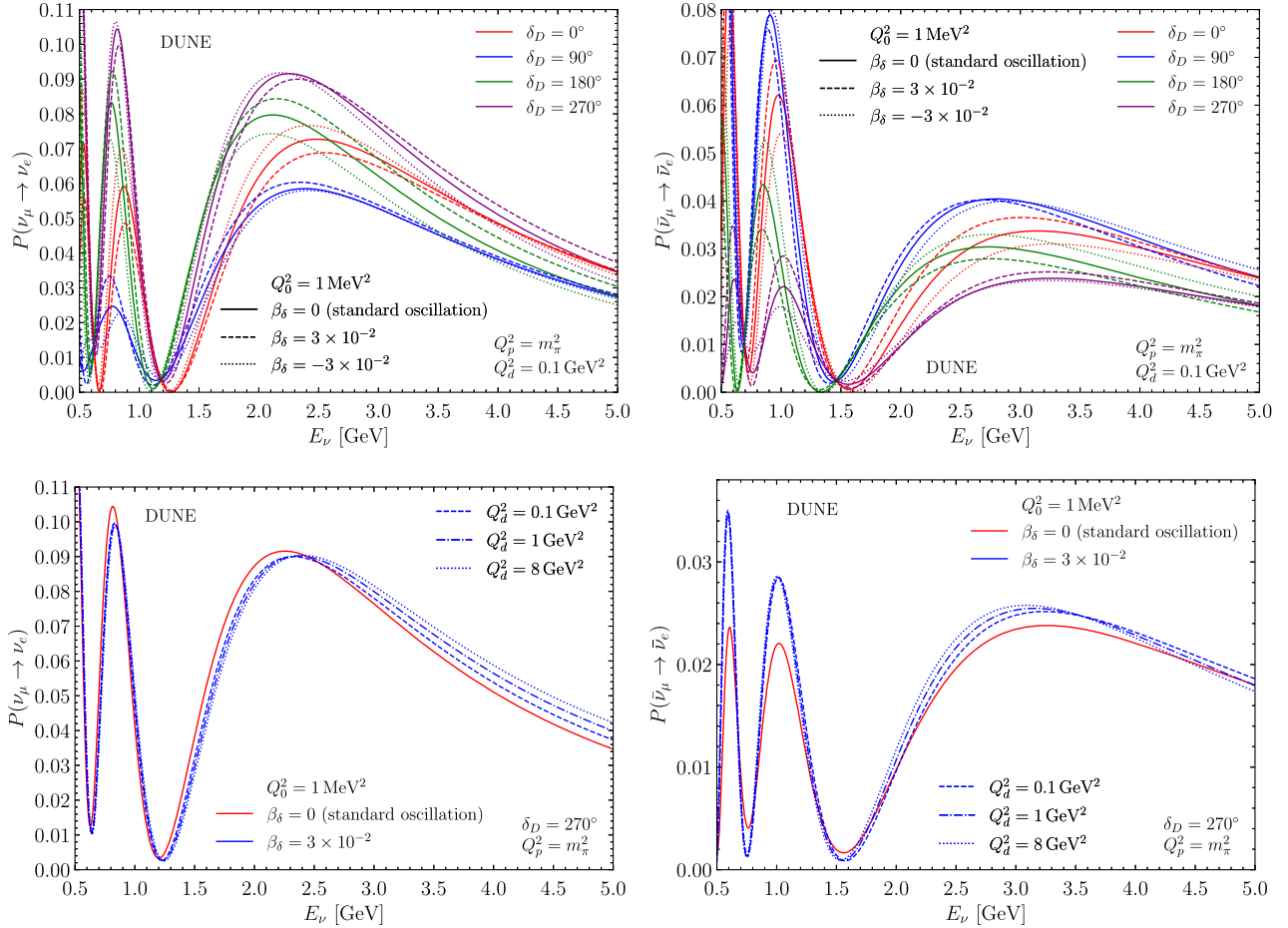
FIG. 3.   The oscillation probabilities as a function of the neutrino energy E_ν for the DUNE configuration with $L = 1284.9$ km and $\rho = 2.848$ g/cm^3. Upper left: the $\nu_\mu \to \nu_e$ oscillation probabilities for the neutrino mode with $\beta_\delta = 0$ (solid), 3×10^{-2} (dashed), and -3×10^{-2} (dotted). Note that $\beta_\delta = 0$ corresponds to the standard oscillation probabilities without RG running effect. Four different CP values $\delta_D = 0°$ (red), $90°$ (blue), $180°$ (green), and $270°$ (purple) are chosen for illustration. Upper right: same as the left but for the antineutrino mode $\bar{\nu}_\mu \to \bar{\nu}_e$. Lower left: the $\nu_\mu \to \nu_e$ oscillation probabilities with fixed CP value $\delta_D = 270°$ for $Q_d^2 = 0.1$ GeV^2 (dashed blue), 1 GeV^2 (dot-dashed blue), and 8 GeV^2 (blue dotted). Lower right: same as the left but for the antineutrino mode $\bar{\nu}_\mu \to \bar{\nu}_e$.

charged lepton energy $E_\ell^{\rm rec}$ and the measured lepton scattering angle $\theta_\ell^{\rm rec}$,

$$Q_{\rm rec}^2 \equiv |(p_\nu^{\rm rec} - p_\ell^{\rm rec})^2| = 2E_\nu^{\rm rec}(E_\ell^{\rm rec} - |{\bf p}_\ell^{\rm rec}|\cos\theta_\ell^{\rm rec}) - m_\ell^2, \quad (4.1)$$

where m_ℓ is the lepton mass. Note that the lepton momentum cannot be directly reconstructed but needs to be obtained from the reconstructed lepton energy, $|{\bf p}_\ell|^{\rm rec} \equiv \sqrt{(E_\ell^{\rm rec})^2 - m_\ell^2}$. In total, three observables (the reconstructed lepton energy $E_\ell^{\rm rec}$, the hadronic energy $E_{\rm had}^{\rm rec}$, and the measured lepton scattering angle $\theta_\ell^{\rm rec}$) are needed.

1. Energy reconstruction

We use GENIE [87,88] to generate the neutrino-argon scattering events and simulate the neutrino energy

reconstruction at DUNE. Note that the neutrino energy does not fully deposit as visible energy and some is missing. In a liquid argon time projection chamber (TPC) such as the DUNE far detectors, the energy is reconstructed via the tracks left by the final-state particles. Those tracks with deposited energy below the detector threshold cannot be measured. Moreover, some final-state particles such as neutrino cannot leave a track and hence is not measurable either. These contribute as missing energy [89]. To precisely reconstruct the neutrino energy, we add a constant value, $\langle E_{\rm mis}\rangle$, as correction to calibrate the energy reconstruction by taking into account the average missing energy, $\langle E_{\rm mis}\rangle = 30$ MeV, 20 MeV, and 20 MeV for the QES, RES, and DIS scattering processes, respectively.

In addition, the charged lepton ($E_\ell^{\rm rec}$) and hadronic ($E_{\rm had}^{\rm rec}$) energies are smeared around their respective true values. The Gaussain smearing resolution of each detectable

TABLE I. The energy resolutions for detectable particles obtained by fitting to the best reconstruction case in [89].

Particle	Energy resolution (σ/E) at DUNE
$\pi^{\pm}$	15%
$e^{\pm}/\gamma$	1.5%
p	p < 400 MeV/c: 4%
	p > 400 MeV/c:
	$10\% \oplus 3.1\%/\sqrt{E}$ [GeV]
n	$40\%/\sqrt{E}$ [GeV]
Other	$5\% \oplus 30\%/\sqrt{E}$ [GeV]

particle is determined by the *best reconstruction case* in [89] as summarized in Table I.

Figure 4 shows the reconstructed spectrum of CC events for 2.5 GeV ν_e and $\bar{\nu}_e$, respectively. Note that the energy reconstruction for the CC-QES process has a better performance than the other two CC-RES and CC-DIS processes, since the deposited energy for CC-QES mostly comes from the charged leptons which have a better resolution than the other particles produced in the RES and DIS processes.

2. Momentum transfer reconstruction in terms of scattering angle

As mentioned above, the production momentum transfer Q_p^2 has fixed value as the pion mass, $Q_p^2 = m_\pi^2$. For the detection momentum transfer Q_d^2, the previous work [75] also uses a fixed value, $Q_d^2 = 2m_N E_\nu^2/(2E_\nu + m_N)$, where m_N is the target nucleon mass. Then a 2.5 GeV neutrino corresponds to $\sqrt{Q_d^2} \approx 1.4$ GeV. However, the momentum transfer of CC events is not fixed but follows a distribution

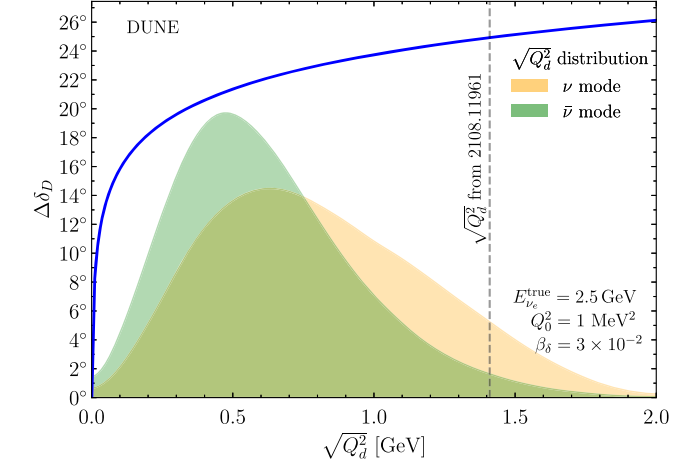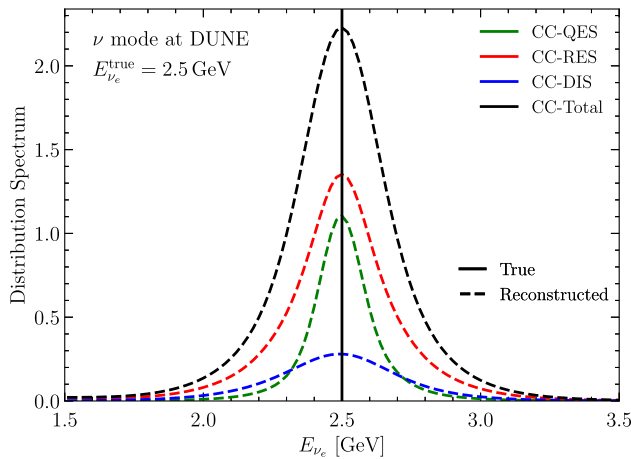FIG. 5. The *CP* phase change $\Delta\delta_D \equiv \beta_\delta \ln(|Q^2/Q_0^2|)$ induced by the RG running effect with $Q_0^2 = 1$ MeV² and $\beta_\delta = 3 \times 10^{-2}$ as function of the detection momentum transfer $\sqrt{Q_d^2}$. The $\sqrt{Q_d^2}$ distributions for ν_e—Argon scattering events are shown with the orange and green shaded regions for the neutrino and antineutrino modes, respectively. For comparison, the fixed $\sqrt{Q_d^2} \approx 1.4$ GeV from $Q_d^2 = 2m_N E_\nu^2/(2E_\nu + m_N)$ is presented by the vertical gray dashed line.

shown as the shaded regions in Fig. 5. The estimated momentum transfer value actually locates at the tail of the distribution and is at least two times of the mean momentum transfer that is around 0.5–0.7 GeV. To see the running effect on the Dirac *CP* phase, we show the *CP* phase change $\Delta\delta_D$ ($\equiv \beta_\delta \ln(|Q^2/Q_0^2|)$) induced by RG running with the blue curve in Fig. 5. The value of $\Delta\delta_D$ varies a lot throughout the $\sqrt{Q_d^2}$ distribution region. Especially for $\sqrt{Q_d^2} < 0.5$ GeV, the corresponding $\Delta\delta_D$ has a large

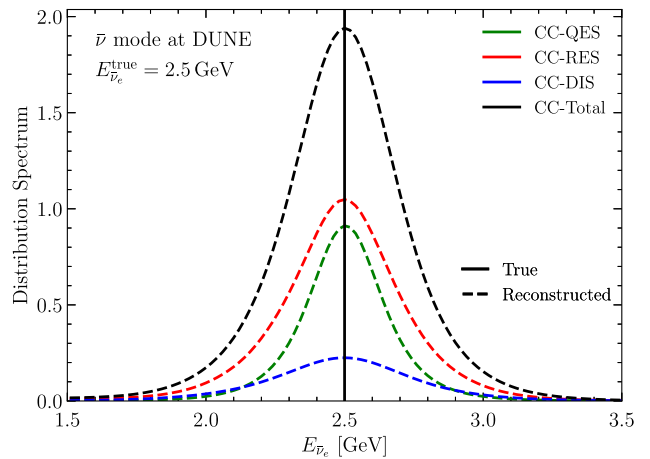FIG. 4. Left: the reconstructed energy ($E_\nu^{rec} = E_\ell^{rec} + E_{had}^{rec}$) distribution of a 2.5 GeV ν_e neutrino at the DUNE detector for different CC scattering processes: QES (green), RES (red), and DIS (blue). The combined total spectrum is plotted in black color. Note that the total spectrum is normalized and the others are weighted by their corresponding cross sections. Right: same as the left panel but for the antineutrino mode.

variation and is quite different from its counterpart adopted in the previous work. Therefore, an event-by-event reconstruction of the detection momentum transfer according to Eq. (4.1) is necessary at DUNE.

In order to reconstruct the detection momentum transfer Q_d^2, the scattering angle reconstruction plays an important role. Note that the Gaussian smearing of the true scattering angle cannot be directly used to simulate the measured angle due to the geometry effect that is illustrated in the left panel of Fig. 6. The incoming neutrino with momentum $\mathbf{p}_\nu$ interacts with the detector target which is marked as the black dot and a final-state

charged lepton with true momentum $\mathbf{p}_\ell^{\text{true}}$ is produced. Since the detector has a limited angular resolution, it measures the lepton momentum $\mathbf{p}_\ell$ with an opening angle $\delta\theta_\ell$ from the true one. The value of $\delta\theta_\ell$ follows a Gaussian distribution that depends on the detector angular resolution σ_θ. In addition, the azimuthal angle ϕ for the measured lepton momentum surrounding the true lepton momentum distributes randomly in $[0, 2\pi)$ and affects the measured lepton scattering angle θ_ℓ^{rec}. We follow the analytical method in [90] where the probability density $P(\theta_\ell^{\text{rec}}|\theta_\ell^{\text{true}})$ for obtaining the measured scattering angle θ_ℓ^{rec} from the given true one $\theta_\ell^{\text{true}}$ is,

$$P(\theta_\ell^{\text{rec}}|\theta_\ell^{\text{true}}) = \frac{1}{2\pi} \int_0^\pi \frac{P(\delta\theta_\ell)\sin\theta_\ell^{\text{rec}}}{\sqrt{\sin^2\theta_\ell^{\text{true}}\sin^2\delta\theta_\ell - (\cos\theta_\ell^{\text{true}}\cos\delta\theta_\ell - \cos\theta_\ell^{\text{rec}})^2}} d\delta\theta_\ell. \qquad (4.2)$$

In the above expression, $P(\delta\theta_\ell) \equiv \sin\delta\theta_\ell/N(\sigma_\theta) \times \exp[-1/2(\delta\theta_\ell/\sigma_\theta)^2]$ is the distribution function of the opening angle $\delta\theta_\ell$ with σ_θ being the detector angular resolution and $N(\sigma_\theta)$ the normalization factor. In our analysis, we take $\sigma_\theta = 1°$ from the DUNE Conceptual Design Report (CDR) result [24]. In the right panel of Fig. 6, we show the probability density for the measured scattering angle θ_ℓ^{rec} with four true scattering angle values $\theta_\ell^{\text{true}} = 0°, 15°, 30°$, and $45°$ for illustration. For $\theta_\ell^{\text{true}} \gg \sigma_\theta$, the smeared scattering angle closely follows a Gaussian distribution while the shape is significantly distorted when the $\theta_\ell^{\text{true}}$ value is comparable with its angular resolution σ_θ.

Finally, the combination of E_ν^{rec}, E_ℓ^{rec}, and θ_ℓ^{rec} through Eq. (4.1) reconstructs the detection momentum transfer

Q_d^2. Figure 7 shows the $\sqrt{Q_d^2}$ distribution of a 2.5 GeV neutrino scattering with Argon target for different CC scattering processes. The reconstructed momentum transfer distributions (dashed) are in good agreement with the true ones (solid), although the neutrino energy reconstruction is far from being perfect as shown in Fig. 4.

3. 4-D transfer table for energy and momentum transfer

As mentioned above, the detector energy and angular resolutions will smear the true values $(E_\nu^{\text{true},i}, Q_{\text{true},j}^2)$ into their reconstructed counterparts $(E_\nu^{\text{rec},i'}, Q_{\text{rec},j'}^2)$ with i, j, i', and j' being the indices of
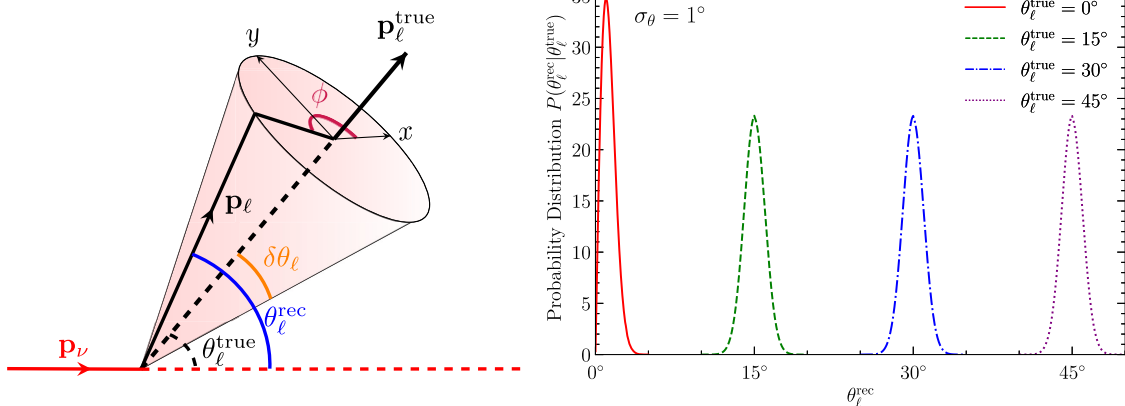

FIG. 6. Left: the schematic plot for the charged lepton scattering angle θ_ℓ^{rec} reconstruction. With $\theta_\ell^{\text{true}}$ being the true scattering angle between the final-state lepton $\mathbf{p}_\ell^{\text{true}}$ and incoming neutrino $\mathbf{p}_\nu$ momenta, $\delta\theta_\ell$ is the opening angle between the measured lepton $\mathbf{p}_\ell$ and the true one $\mathbf{p}_\ell^{\text{true}}$. Moreover, the azimuthal angle ϕ for the measured lepton momentum surrounding the true lepton momentum is randomly distributed in the range of $[0, 2\pi)$. Right: the probability distribution of the lepton scattering angle θ_ℓ^{rec} with four true scattering angles: $\theta_\ell^{\text{true}} = 0°$ (solid red), $15°$ (dashed green), $30°$ (dot-dashed blue), and $45°$ (dotted purple). We use the angular resolution $\sigma_\theta = 1°$ from the DUNE CDR result.
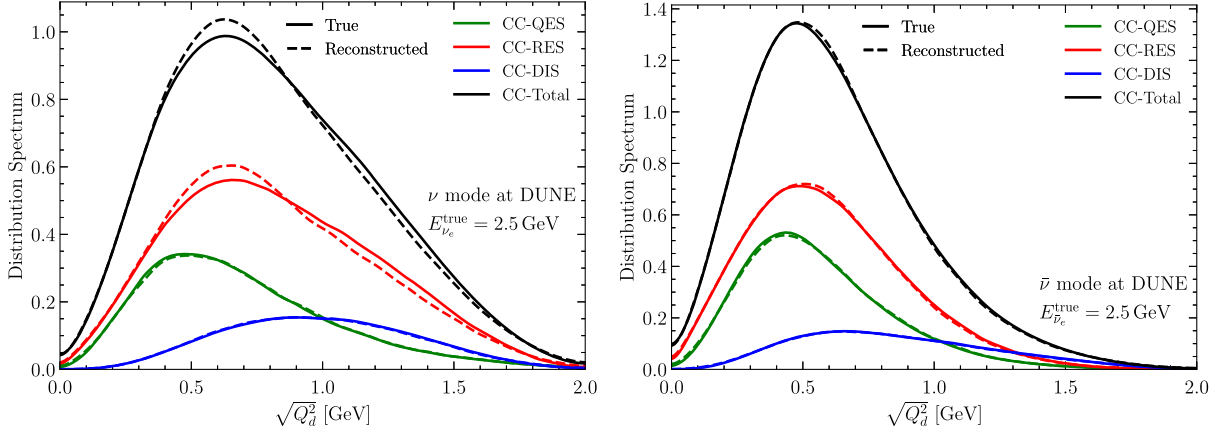
FIG. 7. Left: the reconstructed momentum transfer $\sqrt{Q_d^2}$ distribution of a 2.5 GeV ν_e neutrino at the DUNE detector for different CC scattering processes: QES (green), RES (red), and DIS (blue). The total spectrum (black) is normalized to 1 while the others are weighted by their corresponding cross sections. Right: same as the left panel but for the antineutrino mode.

their respective bins. Given a true neutrino energy and a true momentum transfer, the transfer between the true and reconstructed values is summarized in a 4-D transfer table $T'_{iji'j'}$,

$$T'_{iji'j'} \equiv \frac{\Delta N(E_\nu^{\text{true},i}, Q_{\text{true},j}^2; E_\nu^{\text{rec},i'}, Q_{\text{rec},j'}^2)}{N_{\text{total}}(E_\nu^{\text{true},i}, Q_{\text{true},j}^2)}. \quad (4.3)$$

Here $\Delta N(E_\nu^{\text{true},i}, Q_{\text{true},j}^2; E_\nu^{\text{rec},i'}, Q_{\text{rec},j'}^2)$ is the simulated event number within the i'th reconstructed energy bin and the j'th reconstructed momentum transfer bin for the given ith true neutrino energy bin and the jth true momentum transfer bin, while $N_{\text{total}}(E_\nu^{\text{true},i}, Q_{\text{true},j}^2)$ is the total simulated event number of the given ith true neutrino energy bin and jth true momentum transfer bin. The transfer table element is the probability for finding the reconstructed values $(E_\nu^{\text{rec},i'}, Q_{\text{rec},j'}^2)$ after smearing their respective true values $(E_\nu^{\text{true},i}, Q_{\text{true},j}^2)$. Such effective transfer table satisfies the probability conservation condition, $\sum_{i'j'} T'_{iji'j'} = 1$, as expected. Moreover, the transfer table enters the reconstructed event rates calculation as elaborated below.

B. Extended GLoBES simulation with both energy and momentum transfer

As pointed out around Eq. (3.9), the oscillation probability has momentum transfer dependence. In the presence of the RG running effect, the neutrino oscillation event rate is a function of not just the neutrino energy (E_ν) but also the momentum transfers (Q_p^2 and Q_d^2). With the production momentum transfer (Q_p^2) typically fixed by the parent meson masses, the event rate is still a two-dimensional distribution of the neutrino energy (E_ν) and the detection momentum transfer (Q_d^2).

The GLoBES [91,92] simulation for fixed baseline experiments with one-dimensional event rate needs to be extended in order to incorporate the RG running effect. The two-dimensional binning approach with neutrino energy and zenith angle (baseline length) dependence has been used in the atmospheric neutrino oscillation analysis [93,94]. We adopt similar approach by breaking the 2-D event rate $d^2N/dE_\nu dQ_d^2$ into multiple glb experimental profiles each with a fixed Q_d^2 and merging them in the end.

(i) GLoBES simulation: With a fixed Q_d^2 for each glb profile, the oscillation probability $P_{\alpha\beta}(E_\nu^{\text{true},i}, Q_{\text{true},j}^2)$ with the RG running effect in Sec. III C taken into account and the corresponding event spectrum can be calculated in the usual way by GLoBES,

$$\left.\frac{dN^{\text{true}}}{dE_\nu^{\text{true},i}}\right|_{Q_{\text{true},j}^2}$$
$$\equiv N^{\text{target}}\phi_\alpha(E_\nu^{\text{true},i})P_{\alpha\beta}(E_\nu^{\text{true},i}, Q_{\text{true},j}^2)\sigma_\beta(E_\nu^{\text{true},i}), \quad (4.4)$$

where N^{target} is the normalization factor including the information of running time, detector size, and the baseline length. Both the α-flavor neutrino flux $\phi_\alpha(E_\nu^{\text{true},i})$ and β-flavor detection cross section $\sigma_\beta(E_\nu^{\text{true},i})$ are functions of the true neutrino energy $E_\nu^{\text{true},i}$ for the ith bin.

Since the neutrino energy E_ν and detection momentum transfer Q_d^2 are reconstructed altogether, their smearing interleaves with each other and cannot be separated. So we first extract from GLoBES the event numbers at the true neutrino energy level,

$$\text{GLB}_j: \quad N_i^{\text{GLB}_j} = \left.\frac{dN^{\text{true}}}{dE_\nu^{\text{true},i}}\right|_{Q_{\text{true},j}^2} \Delta E_i^{\text{true},i}, \quad (4.5)$$

for the jth glb experimental profile without smearing.

(ii) Implementing the momentum transfer distribution by hand: Although GLoBES automatically incorporates the total cross section $\sigma(E_\nu^{\text{true},i})$ in the event rate calculation according to Eq. (4.4), the differential spectrum with respect to the momentum transfer Q_d^2 is still missing. One needs to multiply the extracted event rate $N_i^{\text{GLB}_j}$ with a normalized differential cross section $d\sigma_\beta/(\sigma_\beta dQ_{\text{true},j}^2)$ by hand. The event numbers among different glb profiles are then reshuffled into,

$$N_{ij} \equiv N_i^{\text{GLB}_j} \times \left(\frac{d\sigma_\beta}{\sigma_\beta dQ_{\text{true},j}^2} \right) \bigg|_{E_\nu^{\text{true},i}} \Delta Q_{\text{true},j}^2, \qquad (4.6)$$

weighted by the momentum transfer bin size $\Delta Q_{\text{true},j}^2$. The product of the normalized differential cross section and the true momentum transfer bin size can be simulated by GENIE as, $d\sigma_\beta/(\sigma_\beta dQ_{\text{true},j}^2)|_{E_\nu^{\text{true},i}} \Delta Q_{\text{true},j}^2 = \Delta N(E_\nu^{\text{true},i}, Q_{\text{true},j}^2)/N(E_\nu^{\text{true},i})$, as a ratio between the event number within the jth true momentum transfer bin and the total one for a given true energy.

Note that the two variables $N_i^{\text{GLB}_j}$ and N_{ij} have different physical meanings. While $N_i^{\text{GLB}_j}$ is the event number within the ith energy bin for the jth glb profile that carries the momentum transfer dependence in the oscillation probability but no information about the momentum transfer distribution, the event number N_{ij} within the ith energy and jth momentum transfer bin also includes the differential momentum transfer distribution. The essential difference between these two variables is having the momentum transfer distribution or not. Nevertheless, the j index of $N_i^{\text{GLB}_j}$ cannot be simply omitted since the oscillation probability has momentum transfer dependence. To make this tricky point explicit, we add j as an upper index for $N_i^{\text{GLB}_j}$ and a lower one for N_{ij}.

(iii) Detector resolution and smearing: The normalized differential cross section in the 2-D true event rate calculation Eq. (4.6) cannot be automatically carried out in GLoBES and needs to be implemented by hand. In addition, the 4-D transfer table $T'_{iji'j'}$ defined in Eq. (4.3) also needs to be implemented by hand with multiple glb profiles. For convenience, we combine these two terms into a single effective 4-D transfer table,

$$N_{i'j'} \equiv \sum_{ij} N_{ij} \times T'_{iji'j'} \equiv \sum_{ij} N_i^{\text{GLB}_j} \times T_{iji'j'}, \quad (4.7)$$

where $N_{i'j'}$ is the event number in the i'th reconstructed energy and j'th reconstructed momentum transfer bin. Instead of using the $T'_{iji'j'}$ Eq. (4.3), the event rate $N_i^{\text{GLB}_j}$ extracted from GLoBES is directly related to the reconstructed event rate $N_{i'j'}$ with,

$$\begin{aligned} T_{iji'j'} &\equiv \left(\frac{d\sigma_\beta}{\sigma_\beta dQ_{\text{true},j}^2} \right) \bigg|_{E_\nu^{\text{true},i}} \times \Delta Q_{\text{true},j}^2 \times T'_{iji'j'} \\ &= \frac{\Delta N(E_\nu^{\text{true},i}, Q_{\text{true},j}^2; E_\nu^{\text{rec},i'}, Q_{\text{rec},j'}^2)}{N_{\text{total}}(E_\nu^{\text{true},i})}, \end{aligned} \qquad (4.8)$$

where $N_{\text{total}}(E_\nu^{\text{true},i})$ is the total event number for the given ith true neutrino energy bin. The effective transfer table includes three terms: the normalized differential cross section $d\sigma_\beta/(\sigma_\beta dQ_{\text{true},j}^2)|_{E_\nu^{\text{true},i}}$, the bin size $\Delta Q_{\text{true},j}^2$, and the smearing transfer table $T'_{iji'j'}$, which can be combined into a single simulation.

In our simulation, we first use GENIE to generate 10^6 neutrino-Ar scattering events for the true energy $E_\nu^{\text{true},i}$ at the center of each bin. We then reconstruct event by event the neutrino energy and momentum transfer after smearing according to the detector energy and angular resolutions as discussed in Sec. IV A. For the true/reconstructed energy, we take a 0.25 GeV bin size from 0.5 to 5 GeV. On the other hand, the true/reconstructed momentum transfer uses $\sqrt{Q_d^2}$ instead of Q_d^2 with 25 bins from 0 to $2\sqrt{2}$ GeV since Q_d^2 distributes mainly at small values as shown in Fig. 7. Finally, we bin the events into a histogram with variables $(E_\nu^{\text{true}}, Q_{\text{true}}^2; E_\nu^{\text{rec}}, Q_{\text{rec}}^2)$ and divide the event number in each bin by the total event number to obtain the $T_{iji'j'}$ defined in Eq. (4.8). After these, we calculate the 2-D event rates according to Eq. (4.7) and feed them back into GLoBES for χ^2 analysis to take full advantage.

C. Event rate and *CP* phase sensitivity at DUNE

Figure 8 shows the event rates at DUNE as function of the reconstructed neutrino energy E_ν^{rec} (upper panels) or momentum transfer $\sqrt{Q_{\text{rec}}^2}$ (lower panels) for both neutrino (left panels) and antineutrino (right panels) modes. The event rate difference between the thin and thick lines induced by the RG running effect can reach percentage level. This happens for not just the signal (red lines) but the various background event rates since all channels are subject to the oscillation probabilities. The most prominent channel is the beam $\nu_e + \bar{\nu}_e$ background that is modulated by P_{ee}. As pointed out earlier at the end of Sec. III B, P_{ee} is no longer independent of the Dirac *CP* phase δ_D as usually
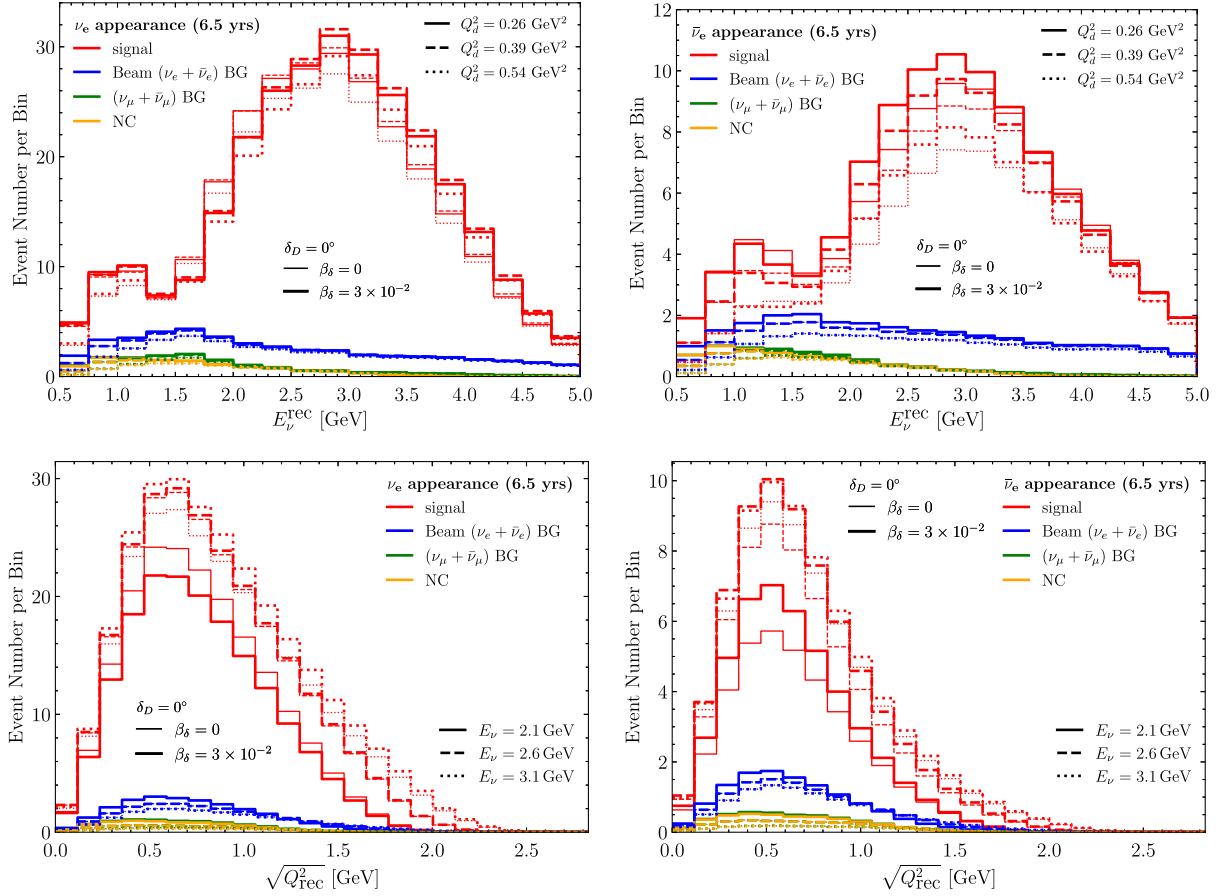
FIG. 8.   Upper panels: the reconstructed appearance event rates as a function of the reconstructed neutrino energy $E_\nu^{\rm rec}$ with detection momentum transfer $Q_d^2 = 0.26$ GeV^2 (solid), 0.39 GeV^2 (dashed), and 0.54 GeV^2 (dotted) for the neutrino ν_e (upper left) and antineutrino $\bar{\nu}_e$ (upper right) modes. Lower panels: the reconstructed appearance event rates as a function of $\sqrt{Q_{\rm rec}^2}$ with $E_\nu =$ 2.125 GeV (solid), 2.625 GeV (dashed), and 3.125 GeV (dotted) for the neutrino ν_e (lower left) and antineutrino $\bar{\nu}_e$ (lower right) modes. For all panels, the event rates are divided into four components: the signal (red), the intrinsic $\nu_e + \bar{\nu}_e$ beam background (blue), the $\nu_\mu + \bar{\nu}_\mu$ beam background (green), and the neutral current background (orange). We take $\delta_D = 0°$ and a 6.5 years of running time for each neutrino and antineutrino mode to make illustration.

expected but becomes a function of the *CP* phase difference $\Delta\delta_D$ induced by the RG running effect. The largest variation occurs in the ranges $[1.5, 4.5]/[1.25, 3.5]$ GeV of $E_\nu^{\rm rec}$ and $[0.2, 1.5]/[0.2, 1.2]$ GeV of $\sqrt{Q_{\rm rec}^2}$ for the neutrino/antineutrino mode, respectively, around the peaks.

To further explore the features induced by the RG running effect, we show the relative difference of the two-dimensional signal event rate, $\Delta N/N \equiv (N_{\rm sig}(\beta_\delta = 3 \times 10^{-2}) - N_{\rm sig}(\beta_\delta = 0))/N_{\rm sig}(\beta_\delta = 0)$, on the $(E_\nu^{\rm rec}, \sqrt{Q_{\rm rec}^2})$ plane in Fig. 9. Note that the distribution of $\Delta N/N$ is quite different between the neutrino (left) and antineutrino (right) modes. For the neutrino mode, the positive $\Delta N/N$ values distribute at $E_\nu^{\rm rec} \in [3.5, 5]$ GeV while the negative one within $E \in [1.5, 2.5]$ GeV. As for the antineutrino mode, the negative $\Delta N/N$ values mainly distribute at $E_\nu^{\rm rec} \in [1, 1.75]$ GeV for most $\sqrt{Q_{\rm rec}^2}$ and

$E_\nu^{\rm rec} \in [3.5, 4.75]$ GeV for $\sqrt{Q_{\rm rec}^2} \in [0, 1.2]$ GeV, with the positive values in the remaining part. The RG running effect can be tested at the future LBL experiments such as DUNE. Unfortunately, since the genuine *CP* phase is undetermined, a degeneracy between the genuine *CP* phase δ_D and the RG running parameter β_δ arises which reduces the *CP* phase sensitivity. The structure in the two-dimensional $(E_\nu^{\rm rec}, \sqrt{Q_{\rm rec}^2})$ distributions may help to disentangle the degeneracy.

To quantify the impact on the *CP* phase sensitivity from the RG running effect at DUNE, we extend the χ^2 function,

$$\chi^2 = \chi_{\rm stat}^2 + \chi_{\rm sys}^2 + \chi_{\rm prior}^2, \qquad (4.9)$$

by incorporating multiple glb profiles. More concretely, the first term $\chi_{\rm stat}^2$ for statistical fluctuations,

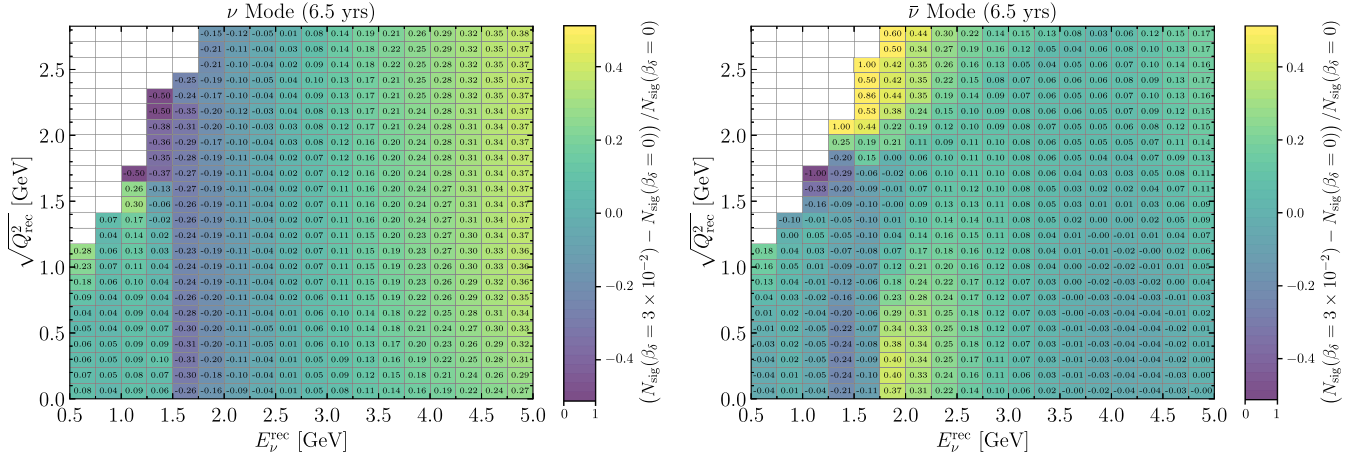FIG. 9. The relative difference, $\Delta N/N \equiv (N_{\rm sig}(\beta_\delta = 3 \times 10^{-2}) - N_{\rm sig}(\beta_\delta = 0))/N_{\rm sig}(\beta_\delta = 0)$, between the two cases with and without the RG running effect in the two-dimensional $E_\nu^{\rm rec}$ and $\sqrt{Q_{\rm rec}^2}$ bins for the neutrino (left) and antineutrino (right) modes. We take $\delta_D = 0°$ and a 6.5 years of running time for each mode.

$$\chi_{\rm stat}^2 = \sum_{i'j'r} \left(\frac{N_{i'j'}^r({\rm true}) - (1+a_r)N_{i'j'}^{r,{\rm sig}}({\rm test}) - (1+b_r)N_{i'j'}^{r,{\rm bkg}}({\rm test})}{\sqrt{N_{i'j'}^r({\rm true})}} \right)^2, \qquad (4.10)$$

needs to sum over not just the two indices i' and j' for the neutrino energy and the momentum transfer but also the third index r for the various rules from each experimental profile. The quantity $N_{i'j'}^{r,{\rm sig}}$ ($N_{i'j'}^{r,{\rm bkg}}$) is the signal (background) event number within the i'th reconstructed energy as well as the j'th reconstructed momentum transfer bin for the rule r and can be calculated with true or test oscillation parameters. We define $N_{i'j'}^r({\rm true}) \equiv N_{i'j'}^{r,{\rm sig}}({\rm true}) + N_{i'j'}^{r,{\rm bkg}}({\rm true})$ to represent the total event numbers of signal and background with the true oscillation parameters. Moreover, a_r and b_r are the signal and background normalization nuisance parameters, respectively, for the rule r.

The $\chi_{\rm sys}^2$ term contains the Gaussian priors of signal and background normalizations. For the signal normalization, we take $\sigma_{\nu_e,\bar{\nu}_e} = 2\%$ and $\sigma_{\nu_\mu,\bar{\nu}_\mu} = 5\%$ for the electron (anti) neutrino and muon (anti)neutrino detection, respectively. A common 5% uncertainty is used for the background normalization. These parameters are taken from the experiment simulation configurations of the DUNE Technical Design Report [95].

The final term $\chi_{\rm prior}^2$ summarizes the prior knowledge on the oscillation parameters. We take their best-fit values from the global fit result [42],

$$\sin^2\theta_s = 0.318, \quad \sin^2\theta_a = 0.574, \quad \sin^2\theta_r = 0.022, \tag{4.11a}$$

$$\Delta m_s^2 = 7.50 \times 10^{-5} \text{ eV}^2, \quad \Delta m_a^2 = 2.55 \times 10^{-3} \text{ eV}^2. \tag{4.11b}$$

Among these oscillation parameters, the solar mass squared difference Δm_s^2 and the solar mixing angle θ_s are fixed in our fit since the oscillation probability variation induced by these two parameters is negligibly small [36]. This feature still applies even in the presence of the RG running effect as we have checked numerically. The reactor mixing angle θ_r, the atmospheric mixing angle θ_a, and the atmospheric mass-squared difference Δm_a^2 are treated as free parameters with priors taken from the marginalized one-dimensional χ^2 curves [42]. Due to large uncertainties and the existing tension between the T2K and NOνA results as mentioned in Sec. I, we do not include any prior on the Dirac CP phase δ_D and simply treat it as a free parameter. Moreover, we take the normal ordering of neutrino masses throughout our study. We first consider a free β_δ while the prior knowledge can be extracted from the SBL experiments as we study in Sec. V.

We perform the χ^2 analysis according to Eq. (4.9) to calculate the DUNE sensitivities to δ_D and β_δ as shown in the left panel of Fig. 10. Based on the true oscillation parameter setup ($\delta_D = 270°$ and $\beta_\delta = 0$) that is marked by a black star, the black contours show the sensitivities at confidence levels of 68% (solid), 90% (dashed), 95% (dotdashed), and 99% (dotted). Those points on the same contour have exactly the same $\Delta\chi^2$ value and hence
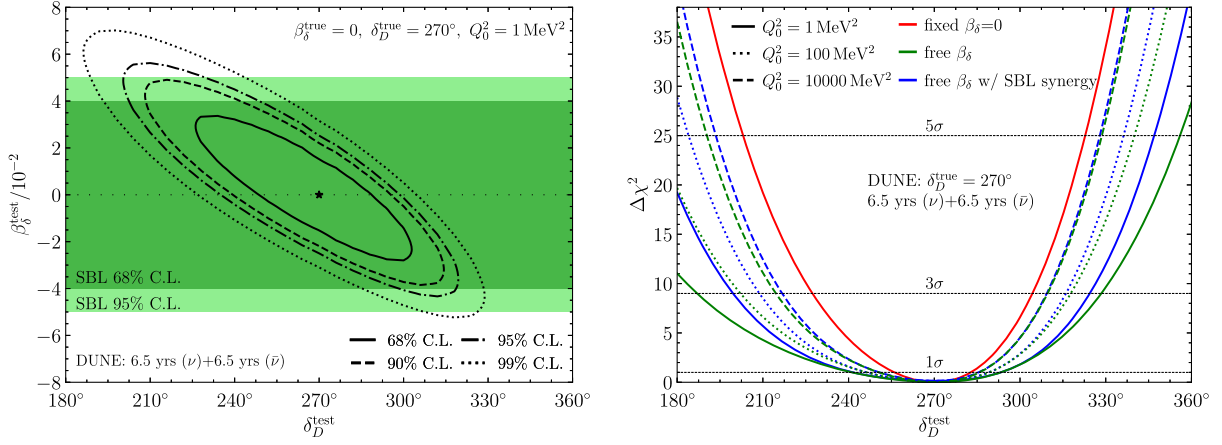
FIG. 10. Left: the two-dimensional sensitivities on δ_D and β_δ at the confidence levels of 68% (solid), 90% (dashed), 95% (dot-dashed), and 99% (dotted) with $Q_0^2 = 1$ MeV^2 and a 6.5 years running time each for the neutrino and antineutrino modes. The true parameter setup $\delta_D^{\text{true}} = 270°$ and $\beta_\delta^{\text{true}} = 0$ is marked by a black star. Moreover, the SBL β_δ constraint at 68% (95%) confidence level is shown by the dark-green (light-green) bands. Right: the marginalized sensitivity to the genuine *CP* phase δ_D with three different prior cases: the fixed $\beta_\delta^{\text{test}} = 0$ (red), a totally free $\beta_\delta^{\text{test}}$ (green), and a free $\beta_\delta^{\text{test}}$ but with the SBL constraint (blue). For comparison, results with $Q_0^2 = 1/100/10000$ MeV^2 are shown as solid/dotted/dashed curves.

degenerate with each other. Since a positive (negative) β_δ can increase (decrease) δ_D according to Eq. (2.2), the combination of a positive β_δ and a smaller δ_D degenerates with a combination of opposite values. This degeneracy correlates the two parameters and makes the sensitivity contours tilt from top left (larger β_δ and smaller δ_D) to bottom right (smaller β_δ and larger δ_D). The tilting behavior implies that the *CP* phase sensitivity would be reduced from the case without RG running. Moreover, there is an asymmetry in the sensitivity contour around the black star. The asymmetry is not caused by the RG running effect since it already exists between the intersection points of the contours and the horizontal line for $\beta_\delta^{\text{test}} = 0$. In fact, it arises from the matter effect while the RG running case inherits and enlarges this asymmetry which can also been seen from the right panel.

To clearly see the impact of RG running on the *CP* phase sensitivity, the marginalized $\Delta\chi^2$ is shown in the right panel of Fig. 10. The red curve with a fixed $\beta_\delta^{\text{test}} = 0$ corresponds to the standard oscillation case without RG running while the green one sets $\beta_\delta^{\text{test}}$ free. From the red to the green curves, the *CP* phase sensitivity significantly reduces. The original 1σ interval of $\sim[255°, 283°]$ changes to $\sim[240°, 295°]$ with almost a factor of 2 reduction.

Moreover, we investigate the effect of the reference momentum transfer Q_0^2 by considering three different values: $Q_0^2 = 1$ MeV^2 (solid), 100 MeV^2 (dotted), and 10000 MeV^2 (dashed). Although the *CP* phase sensitivity increases with Q_0^2 since the distance from the actual momentum transfer Q_d^2 decreases to reduce the RG running effect, the impact on the *CP* measurement at DUNE still cannot be neglected even for $Q_0^2 = 10000$ MeV^2. Therefore, there exists a large parameter space for the

energy scale of new physics that can significantly affect the leptonic *CP* phase sensitivity.

V. SYNERGY WITH EXISTING SHORT-BASELINE EXPERIMENTS

In the zero-distance limit, the probability of flavor transition induced by the RG running effect depends on the *CP* phase difference $\Delta\delta_D$ instead of the genuine *CP* phase δ_D as shown in Eq. (3.13). Hence SBL experiments can provide a clean measurement for RG running. Therefore, a synergy between the long- and short-baseline experiments can disentangle the genuine *CP* phase (δ_D) from the RG running effect (β_δ).

The searches for neutrino transition in the zero-distance limit are done by $\mathcal{O}(100$ m) SBL experiments such as ICARUS [96], CHARM-II [97], NOMAD [98], and NuTeV [99]. All these four experiments use both ν_μ and ν_e neutrinos as well as the antineutrino counterparts. Since ICARUS has only 4 detected ν_e events from the result [96], we will not take it into account due to lack of statistical significance. As for the other three (CHARM-II, NOMAD, and NuTeV), $\mathcal{O}(1000)\nu_e$ events are detected at each experiment [97–99]. Note that antineutrinos are also detected at CHARM-II and NuTeV. Since the antineutrino case is similar to the neutrino one, we just discuss the neutrino case at SBL experiments for illustration in the following text. These ν_e neutrinos are from two sources: the ν_e disappearance from the ν_e flux and those from the $\nu_\mu \rightarrow \nu_e$ transition due to the zero-distance effect. The experimental constraint on the $\nu_\mu \rightarrow \nu_e$ transition probability can be obtained by comparing the predicted ν_e neutrino spectra with the experimental data. Besides the $\nu_\mu \rightarrow \nu_e$ transition, these SBL experiments can also search
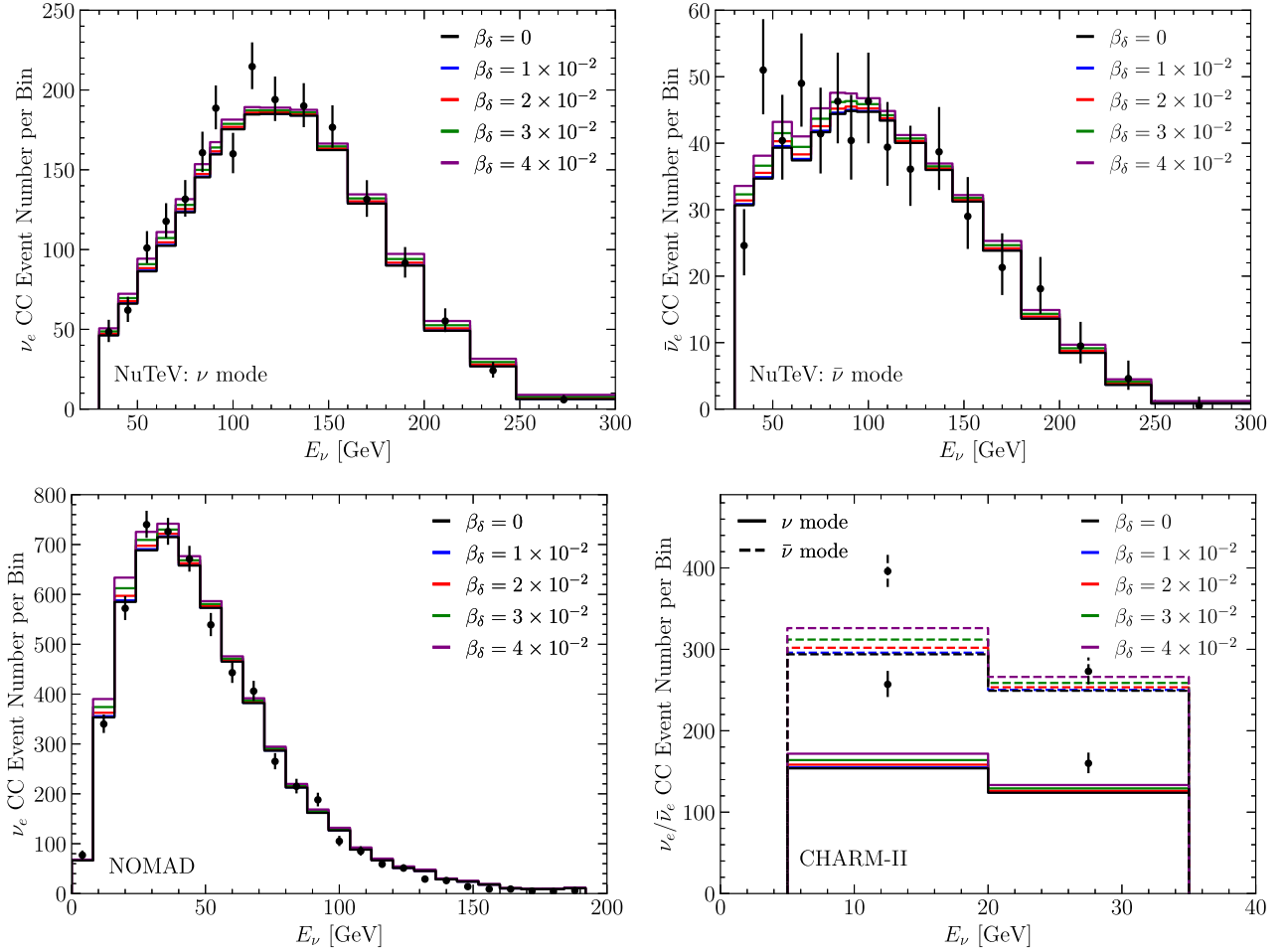
FIG. 11. The $\nu_e/\bar{\nu}_e$ CC event rates for NuTeV with the neutrino mode (upper left), NuTeV with the antineutrino mode (upper right), NOMAD with the neutrino mode (lower left), and CHARM-II with both modes (lower right), respectively. Besides the data points (black dot with error bar), the RG running effect is shown with $\beta_\delta = 0$ (black), 1×10^{-2} (blue), 2×10^{-2} (red), 3×10^{-2} (green), and 4×10^{-2} (purple).

for $\nu_e \to \nu_\tau$ as well as $\nu_\mu \to \nu_\tau$ [100–102]. However, since the charged τ lepton produced from ν_τ CC scattering decays immediately into final-state particles such as e, μ, π, and K that can also be produced in other CC or NC events, the detection of ν_τ suffers from these potential backgrounds. Moreover, the τ selection criteria include much more kinematic requirements than its counterparts of e, which needs more complicated analysis. The SBL experiments find no evidence of ν_τ with large background uncertainties. Hence we do not consider such $\nu_{e,\mu} \to \nu_\tau$ transition channels in our current study.

To obtain the experimental constraint on β_δ, we first calculate the predicted ν_e event rate with the RG running effect. For a neutrino experiment, the predicted ν_e event rate can be described as $N_{\nu_e} = A \sum_\alpha \phi(\nu_\alpha) P_{\alpha e} \sigma(\nu_e)$ with A being the coefficient that is related to the experimental efficiencies and reconstruction errors of the detector, $\phi(\nu_\alpha)$ the α flavor neutrino flux, $P_{\alpha e}$ the $\nu_\alpha \to \nu_e$ oscillation probability, and $\sigma(\nu_e)$ the cross section for scattering

between ν_e and target. The predicted ν_e event rate $R(\nu_e)$ from the collaboration [97–99] was obtained by assuming no oscillation, $P_{\alpha e} = \delta_{\alpha e}$. As for the case with RG running, we calculate the predicted ν_e event rates $R'(\nu_e)$ by multiplying the transition probability in Eq. (3.13) with the ν_e and ν_μ MC neutrino event rates [$R(\nu_e)$ and $R(\nu_\mu)$], $R'(\nu_e) \equiv P_{\nu_e \to \nu_e} R(\nu_e) + P_{\nu_\mu \to \nu_e} R(\nu_\mu)$. We take $\sigma(\nu_e) \approx \sigma(\nu_\mu)$ since the neutrino energy is much larger than the charged lepton masses.

Note that the transition probabilities $P_{\nu_e \to \nu_e}$ and $P_{\nu_\mu \to \nu_e}$ with the RG running effect are Q_d^2 dependent as discussed in Sec. III. So the typical high-energy neutrinos at SBL experiments have the advantage of producing large momentum transfer to enhance the RG running effect. However, there is no such momentum transfer information in the published SBL experimental data [97–99]. So in the transition probability calculation, we take the averaged oscillation probability by integrating Eq. (3.13) over the Q_d^2 distribution extracted from the GENIE simulation.

Figure 11 shows the predicted electron-flavor neutrino event rates as well as the experimental data from NuTeV, NOMAD, and CHARM-II. For all experiments, the predicted event rates with a percentage level β_δ are roughly $\mathcal{O}(10\%)$ more than the MC prediction without flavor transition. Note that flipping the sign of β_δ does not affect the predicted event rates since β_δ only appears as the squared term $\sin^2(\Delta\delta_D/2)$ in Eq. (3.13). Such variations are comparable with the experimental uncertainties which means the

experimental sensitivity to β_δ can reach percentage level. Moreover, with the predicted event rates being a linear combination of both the ν_e MC neutrino event rate $R(\nu_e)$ and the ν_μ counterpart $R(\nu_\mu)$, the largest variation between the predicted and expected event rates does not exactly occur at the ν_e event rate peak position since the ν_e and ν_μ fluxes peak at different energies [97–99].

To obtain the sensitivity on β_δ, we consider the following χ^2 function,

$$\chi^2 \equiv \sum_{i=1}^{n_{\text{bins}}} \left(\frac{N^{\text{data},i} - (1+b^e)N_{\nu_e\to\nu_e}^{\text{fit},i} - (1+b^\mu)N_{\nu_\mu\to\nu_e}^{\text{fit},i}}{\sqrt{N^{\text{data},i} + (N_{\nu_e\to\nu_e}^{\text{fit},i}\sigma_i^e)^2 + (N_{\nu_\mu\to\nu_e}^{\text{fit},i}\sigma_i^\mu)^2}} \right)^2 + \left(\frac{b^e}{\sigma_e}\right)^2 + \left(\frac{b^\mu}{\sigma_\mu}\right)^2, \tag{5.1}$$

where $N^{\text{data},i}$ and $N_{\nu_\alpha\to\nu_e}^{\text{fit},i}$ are the experimental data and predicted event number in the ith energy bin, respectively. The nuisance parameter b^e (b^μ) describes the total normalization uncertainty σ_e (σ_μ) for the electron-flavor (muon-flavor) neutrino flux. Moreover, the parameters σ_i^e and σ_i^μ are the systematic uncertainties in each energy bin [97,99,103]. We obtain the constraint on β_δ by minimizing χ^2 over the nuisance parameters and subtracting the global minimum value $\chi^2_{\min}$, $\Delta\chi^2 \equiv \chi^2 - \chi^2_{\min}$, as shown in Fig. 12. For NuTeV with both ν (dashed blue) and $\bar\nu$ modes (dot-dashed green), the $\Delta\chi^2$ curve is flat in the region of $|\beta_\delta| \lesssim 4 \times 10^{-2}$, but raises quickly at larger values. The NOMAD experiment (dotted orange) is more sensitive to smaller $|\beta_\delta|$ than NuTeV with higher

statistics. For NOMAD and the ν mode at NuTeV, the $\Delta\chi^2$ minimum lies at $\beta_\delta = 0$, while the $\bar\nu$ mode at NuTeV slightly prefers a nonzero β_δ. Moreover, the CHARM-II experiment (solid red) disfavors $\beta_\delta = 0$ by $\sim 2\sigma$ since the observed data points have an excess over the expected event rates as shown in Fig. 11. Note that all these $\Delta\chi^2$ curves are symmetric around $\beta_\delta = 0$ since the predicted event rates do not depend on the sign of β_δ as explained before. The combined result (solid black) of these experiments gives a bound of $|\beta_\delta| \lesssim 4 \times 10^{-2}$ (5×10^{-2}) at 68% (95%) confidence level with the best fit being $|\beta_\delta| \approx 2.5 \times 10^{-2}$.

For comparison, we show the 68% and 95% sensitivities on β_δ as dark- and light-green bands in the left panel of Fig. 10. Since the β_δ sensitivities at SBL experiments is actually comparable with the one at DUNE, their synergy should further improve the sensitivity. As the SBL experiments (NuTeV, NOMAD, and CHARM-II) already have existing data, their constraints on β_δ can be treated as priors. The $\Delta\chi^2$ curves shown in the right panel of Fig. 10 does improve after taking the SBL priors into consideration. Note that the current priors at SBL experiments are obtained without considering the momentum transfer distribution due to lack of information. A more detailed analysis with full data from the experimental side should significantly enhance the existing priors.
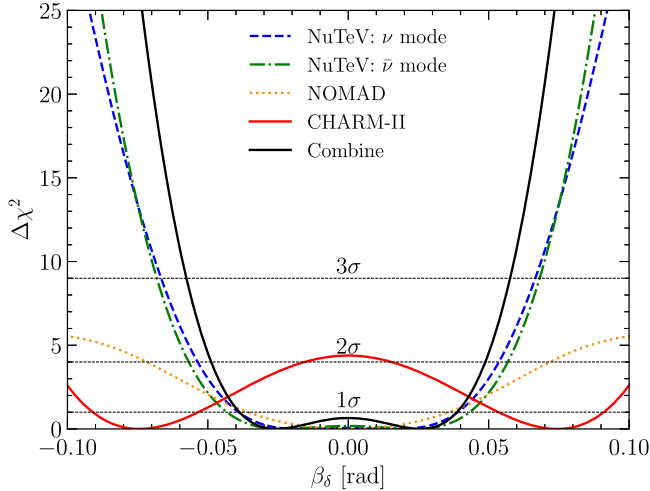

FIG. 12. The $\Delta\chi^2$ ($\equiv\chi^2 - \chi^2_{\min}$) as a function of β_δ for NuTeV with the neutrino mode (dashed blue), NuTeV with the antineutrino mode (dot-dashed green), NOMAD with the neutrino mode (dotted orange), CHARM-II with both neutrino and antineutrino modes (solid red), and their combination (solid black). Moreover, the 1σ, 2σ, and 3σ confidence levels are shown by horizontal black dotted lines.

VI. CONCLUSION AND DISCUSSION

We establish a general and complete formalism for studying the RG running effect on the neutrino oscillation. Especially, our formalism allows an energy dependent momentum transfer for the forward scattering and hence the matter potential. With a broad momentum transfer distribution instead of a single fixed value, our study shows that the degeneracy between the RG running parameter β_δ and the genuine *CP* phase δ_D will significantly reduce the

CP phase sensitivity at DUNE. With mismatch between the momentum transfers in the neutrino production and detection processes, the transition probability of the appearance channels does not vanish even in the limit of zero distance. Consequently, the short-baseline experiments can provide an independent measurement of the RG running parameter β_δ and its synergy with the long-baseline DUNE can help to disentangle the degeneracy and restore the CP phase sensitivity to some extent. Due to lack of information on the momentum transfer, the β_δ sensitivity at short-baseline experiments (NuTeV, NOMAD, and CHARM-II) is comparable with the one at DUNE. We expect more

disentangling capability with full data and detailed analysis from the experimental side.

ACKNOWLEDGMENTS

[1] L. Canetti, M. Drewes, and M. Shaposhnikov, Matter and antimatter in the Universe, New J. Phys. **14,** 095012 (2012).

[2] A. D. Sakharov, Violation of CP invariance, C asymmetry, and baryon asymmetry of the universe, Pis'ma Zh. Eksp. Teor. Fiz. **5,** 32 (1967).

[3] M. B. Gavela, P. Hernandez, J. Orloff, and O. Pene, Standard model CP violation and baryon asymmetry, Mod. Phys. Lett. A **9,** 795 (1994).

[4] P. Huet and E. Sather, Electroweak baryogenesis and standard model CP violation, Phys. Rev. D **51,** 379 (1995).

[5] M. B. Gavela, P. Hernandez, J. Orloff, O. Pene, and C. Quimbay, Standard model CP violation and baryon asymmetry. Part 2: Finite temperature, Nucl. Phys. **B430,** 382 (1994).

[6] M. Fukugita and T. Yanagida, Baryogenesis without grand unification, Phys. Lett. B **174,** 45 (1986).

[7] W. Buchmuller, R. D. Peccei, and T. Yanagida, Leptogenesis as the origin of matter, Annu. Rev. Nucl. Part. Sci. **55,** 311 (2005).

[8] S. Davidson, E. Nardi, and Y. Nir, Leptogenesis, Phys. Rep. **466,** 105 (2008).

[9] M. C. Gonzalez-Garcia and M. Yokoyam, Neutrino masses, mixing, and oscillations, (Chapter 14) of R. L. Workman *et al.* (Particle Data Group), Review of particle physics, Prog. Theor. Exp. Phys. **2022,** 083C01 (2022).

[10] S. Pascoli, S. T. Petcov, and A. Riotto, Connecting low energy leptonic CP-violation to leptogenesis, Phys. Rev. D **75,** 083511 (2007).

[11] G. C. Branco, R. Gonzalez Felipe, and F. R. Joaquim, A new bridge between leptonic CP violation and leptogenesis, Phys. Lett. B **645,** 432 (2007).

[12] S. Pascoli, S. T. Petcov, and A. Riotto, Leptogenesis and low energy CP violation in neutrino physics, Nucl. Phys. **B774,** 1 (2007).

[13] A. Anisimov, S. Blanchet, and P. Di Bari, Viability of Dirac phase leptogenesis, J. Cosmol. Astropart. Phys. 04 (2008) 033.

[14] E. Molinaro and S. T. Petcov, The interplay between the "low" and "high" energy CP-violation in leptogenesis, Eur. Phys. J. C **61,** 93 (2009).

[15] Shao-Feng Ge, Hong-Jian He, and Fu-Rong Yin, Common origin of soft mu-tau and CP breaking in neutrino seesaw and the origin of matter, J. Cosmol. Astropart. Phys. 05 (2010) 017.

[16] M. J. Dolan, T. P. Dutka, and R. R. Volkas, Dirac-phase thermal leptogenesis in the extended type-I seesaw model, J. Cosmol. Astropart. Phys. 06 (2018) 012.

[17] M. A. Acero *et al.* (NOvA Collaboration), First measurement of neutrino oscillation parameters using neutrinos and antineutrinos by NOvA, Phys. Rev. Lett. **123,** 151803 (2019).

[18] K. Abe *et al.* (T2K Collaboration), Constraint on the matter–antimatter symmetry-violating phase in neutrino oscillations, Nature (London) **580,** 339 (2020); **583,** E16 (2020).

[19] D. S. Ayres *et al.* (NOvA Collaboration), NOvA: Proposal to build a 30 kiloton off-axis detector to study $\nu_\mu \to \nu_e$ oscillations in the NuMI beamline, arXiv:hep-ex/0503053.

[20] K. Abe *et al.* (T2K Collaboration), The T2K experiment, Nucl. Instrum. Methods Phys. Res., Sect. A **659,** 106 (2011).

[21] M. A. Acero *et al.* (NOvA Collaboration), Improved measurement of neutrino oscillation parameters by the NOvA experiment, Phys. Rev. D **106,** 032004 (2022).

[22] M. A. Ramírez *et al.* (T2K Collaboration), Measurements of neutrino oscillation parameters from the T2K experiment using 3.6×10^{21} protons on target, Eur. Phys. J. C **83,** 782 (2023).

[23] K. Abe, T. Abe, H. Aihara, Y. Fukuda, Y. Hayato, K. Huang, A. K. Ichikawa, M. Ikeda, K. Inoue, H. Ishino *et al.*, Letter of intent: The hyper-Kamiokande experiment—Detector design and physics potential—, arXiv:1109.3262.

[24] R. Acciarri *et al.* (DUNE Collaboration), Long-baseline neutrino facility (LBNF) and deep underground neutrino experiment (DUNE): Conceptual design report, volume 2: The physics program for DUNE at LBNF, arXiv:1512 .06148.

[25] K. Abe *et al.* (Hyper-Kamiokande Collaboration), Hyper-Kamiokande design report, arXiv:1805.04163.

[26] A. Abud Abed *et al.* (DUNE Collaboration), Low exposure long-baseline neutrino oscillation sensitivity of the DUNE experiment, Phys. Rev. D **105,** 072006 (2022).

[27] A. Alekou *et al.* (ESSnuSB Collaboration), Updated physics performance of the ESSnuSB experiment: ESSnuSB collaboration, Eur. Phys. J. C **81**, 1130 (2021).

[28] K. Abe *et al.* (Hyper-Kamiokande Collaboration), Physics potentials with the second Hyper-Kamiokande detector in Korea, Prog. Theor. Exp. Phys. **2018**, 063C01 (2018).

[29] J. Tang, S. Vihonen, and T. C. Wang, Precision measurements on δ_{CP} in MOMENT, J. High Energy Phys. 12 (2019) 130.

[30] A. V. Akindinov, E. G. Anassontzis, G. Anton, M. Ardid, J. Aublin, B. Baret, V. Bertin, S. Bourret, C. Bozza, M. Bruchner *et al.*, Letter of interest for a neutrino beam from Protvino to KM3NeT/ORCA, Eur. Phys. J. C **79**, 758 (2019).

[31] J. Alonso, F. T. Avignone, W. A. Barletta, R. Barlow, H. T. Baumgartner, A. Bernstein, E. Blucher, L. Bugel, L. Calabretta, L. Camilleri *et al.*, Expression of interest for a novel search for *CP* violation in the neutrino sector: DAEdALUS, arXiv:1006.0260.

[32] Jarah Evslin, Shao-Feng Ge, and Kaoru Hagiwara, The leptonic *CP* phase from T2(H)K and μ^+ decay at rest, J. High Energy Phys. 02 (2016) 137; Shao-Feng Ge, Measuring the leptonic Dirac *CP* phase with TNT2K, in *NuPhys2016: Prospects in Neutrino Physics* (Barbican Centre, London, United Kingdom, 2016), arXiv:1704.08518.

[33] E. Ciuffoli, J. Evslin, and X. Zhang, The leptonic *CP* phase from muon decay at rest with two detectors, J. High Energy Phys. 12 (2014) 051.

[34] E. Ciuffoli, J. Evslin, and F. Zhao, Neutrino physics with accelerator driven subcritical reactors, J. High Energy Phys. 01 (2016) 004.

[35] M. V. Smirnov, Z. J. Hu, S. J. Li, and J. J. Ling, The possibility of leptonic *CP*-violation measurement with JUNO, Nucl. Phys. **B931**, 437 (2018).

[36] Shao-Feng Ge, Chui-Fan Kong, and Pedro Pasquini, Improving *CP* measurement with THEIA and muon decay at rest, Eur. Phys. J. C **82**, 572 (2022).

[37] S. Razzaque and A. Y. Smirnov, Super-PINGU for measurement of the leptonic *CP*-phase with atmospheric neutrinos, J. High Energy Phys. 05 (2015) 139.

[38] S. Razzaque and A. Y. Smirnov, Super-PINGU for measuring *CP* violation, Nucl. Part. Phys. Proc. **265–266**, 183 (2015).

[39] J. Hofestädt, M. Bruchner, and T. Eberl, Super-ORCA: Measuring the leptonic *CP*-phase with atmospheric neutrinos and beam neutrinos, Proc. Sci. ICRC2019 (**2020**) 911.

[40] F. An *et al.* (JUNO Collaboration), Neutrino physics with JUNO, J. Phys. G **43**, 030401 (2016).

[41] K. J. Kelly, P. A. Machado, I. Martinez Soler, S. J. Parke, and Y. F. Perez Gonzalez, Sub-GeV atmospheric neutrinos and *CP*-violation in DUNE, Phys. Rev. Lett. **123**, 081801 (2019).

[42] P. F. de Salas, D. V. Forero, S. Gariazzo, P. Martínez-Miravé, O. Mena, C. A. Ternes, M. Tórtola, and J. W. F. Valle, 2020 global reassessment of the neutrino oscillation picture, J. High Energy Phys. 02 (2021) 071. See tables in the Valencia neutrino global fit.

[43] M. C. Gonzalez-Garcia, M. Maltoni, and T. Schwetz, NuFIT: Three-flavour global analyses of neutrino oscillation experiments, Universe **7**, 459 (2021).

[44] V. De Romeri, E. Fernandez-Martinez, and M. Sorel, Neutrino oscillations at DUNE with improved energy reconstruction, J. High Energy Phys. 09 (2016) 030.

[45] S. K. Raut, Matter effects at the T2HK and T2HKK experiments, Phys. Rev. D **96**, 075029 (2017).

[46] K. J. Kelly and S. J. Parke, Matter density profile shape effects at DUNE, Phys. Rev. D **98**, 015025 (2018).

[47] S. F. King, S. Molina Sedgwick, S. J. Parke, and N. W. Prouse, Effects of matter density profiles on neutrino oscillations for T2HK and T2HKK, Phys. Rev. D **101**, 076019 (2020).

[48] Y. Farzan and M. Tortola, Neutrino oscillations and nonstandard interactions, Front. Phys. **6**, 10 (2018).

[49] P. S. Bhupal Dev, K. S. Babu, P. B. Denton, P. A. N. Machado, C. A. Argüelles, J. L. Barrow, S. S. Chatterjee, M. C. Chen, A. de Gouvêa, B. Dutta *et al.*, Neutrino nonstandard interactions: A status report, SciPost Phys. Proc. **2**, 001 (2019).

[50] Shao-Feng Ge and Alexei Y. Smirnov, Non-standard interactions and the *CP* phase measurements in neutrino oscillations at low energies, J. High Energy Phys. 10 (2016) 138.

[51] Shao-Feng Ge, The leptonic *CP* measurement and new physics alternatives, Proc. Sci. NuFact2019 (**2020**) 108; New physics with scalar and dark non-standard interactions in neutrino oscillation, J. Phys. Conf. Ser. **1468**, 012125 (2020).

[52] P. Bakhti and M. Rajaee, Sensitivities of future reactor and long-baseline neutrino experiments to NSI, Phys. Rev. D **103**, 075003 (2021).

[53] S. S. Chatterjee, P. S. B. Dev, and P. A. N. Machado, Impact of improved energy resolution on DUNE sensitivity to neutrino non-standard interactions, J. High Energy Phys. 08 (2021) 163.

[54] A. Medhi, D. Dutta, and M. M. Devi, Exploring the effects of scalar nonstandard interactions on the *CP* violation sensitivity at DUNE, J. High Energy Phys. 06 (2022) 129.

[55] A. Medhi, M. M. Devi, and D. Dutta, Imprints of scalar NSI on the *CP*-violation sensitivity using synergy among DUNE, T2HK and T2HKK, J. High Energy Phys. 01 (2023) 079.

[56] J. S. Diaz, Neutrinos as probes of Lorentz invariance, Adv. High Energy Phys. **2014**, 962410 (2014).

[57] M. D. C. Torri, Neutrino oscillations and Lorentz invariance violation, Universe **6**, 37 (2020).

[58] H. X. Lin, J. Tang, S. Vihonen, and P. Pasquini, Nonminimal Lorentz invariance violation in light of the muon anomalous magnetic moment and long-baseline neutrino oscillation data, Phys. Rev. D **105**, 096029 (2022).

[59] R. Majhi, S. Chembra, and R. Mohanta, Exploring the effect of Lorentz invariance violation with the currently running long-baseline experiments, Eur. Phys. J. C **80**, 364 (2020).

[60] S. Kumar Agarwalla and M. Masud, Can Lorentz invariance violation affect the sensitivity of deep underground neutrino experiment?, Eur. Phys. J. C **80**, 716 (2020).

[61] N. Fiza, N. R. Khan Chowdhury, and M. Masud, Investigating Lorentz invariance violation with the long baseline experiment P2O, J. High Energy Phys. 01 (2023) 076.

[62] D. V. Forero, S. Morisi, M. Tortola, and J. W. F. Valle, Lepton flavor violation and non-unitary lepton mixing in low-scale type-I seesaw, J. High Energy Phys. 09 (2011) 142.

[63] F. J. Escrihuela, D. V. Forero, O. G. Miranda, M. Tortola, and J. W. F. Valle, On the description of nonunitary neutrino mixing, Phys. Rev. D **92**, 053009 (2015); **93**, 119905(E) (2016).

[64] Shao-Feng Ge, Pedro Pasquini, M. Tortola, and J. W. F. Valle, Measuring the leptonic *CP* phase in neutrino oscillations with nonunitary mixing, Phys. Rev. D **95**, 033005 (2017).

[65] P. Pasquini, S. F. Ge, M. A. Tórtola, and J. W. F. Valle, Measuring the leptonic *CP* phase in neutrino oscillations with non-unitary mixing, Proc. Sci. NOW2016 (**2017**) 026.

[66] F. J. Escrihuela, D. V. Forero, O. G. Miranda, M. Tórtola, and J. W. F. Valle, Probing *CP* violation with non-unitary mixing in long-baseline neutrino oscillation experiments: DUNE as a case study, New J. Phys. **19**, 093005 (2017).

[67] D. V. Forero, C. Giunti, C. A. Ternes, and M. Tortola, Nonunitary neutrino mixing in short and long-baseline experiments, Phys. Rev. D **104**, 075030 (2021).

[68] I. Martinez-Soler and H. Minakata, Standard versus non-standard *CP* phases in neutrino oscillation in matter with non-unitarity, Prog. Theor. Exp. Phys. **2020**, 063B01 (2020).

[69] J. Huang and S. Zhou, The Mikheyev-Smirnov-Wolfenstein matter potential at the one-loop level in the standard model, Phys. Rev. D **108**, 093010 (2023).

[70] J. A. Casas, J. R. Espinosa, A. Ibarra, and I. Navarro, General RG equations for physical neutrino parameters and their phenomenological implications, Nucl. Phys. **B573**, 652 (2000).

[71] P. H. Chankowski and S. Pokorski, Quantum corrections to neutrino masses and mixing angles, Int. J. Mod. Phys. A **17**, 575 (2002).

[72] S. Antusch, J. Kersten, M. Lindner, and M. Ratz, Running neutrino masses, mixings and *CP* phases: Analytical results and phenomenological consequences, Nucl. Phys. **B674**, 401 (2003).

[73] S. Ray, Renormalization group evolution of neutrino masses and mixing in seesaw models: A review, Int. J. Mod. Phys. A **25**, 4339 (2010).

[74] T. Ohlsson and S. Zhou, Renormalization group running of neutrino parameters, Nat. Commun. **5**, 5153 (2014).

[75] K. S. Babu, V. Brdar, A. de Gouvêa, and P. A. N. Machado, Energy-dependent neutrino mixing parameters at oscillation experiments, Phys. Rev. D **105**, 115014 (2022).

[76] M. Gell-Mann and F. E. Low, Quantum electrodynamics at small distances, Phys. Rev. **95**, 1300 (1954).

[77] X. G. Wu, S. J. Brodsky, and M. Mojaza, The renormalization scale-setting problem in QCD, Prog. Part. Nucl. Phys. **72**, 44 (2013).

[78] M. Bustamante, A. M. Gago, and J. Jones Perez, SUSY renormalization group effects in ultra high energy neutrinos, J. High Energy Phys. 05 (2011) 133.

[79] K. S. Babu, V. Brdar, A. de Gouvêa, and P. A. N. Machado, Addressing the short-baseline neutrino anomalies with energy-dependent mixing parameters, Phys. Rev. D **107**, 015017 (2023).

[80] K. S. Babu, C. N. Leung, and J. T. Pantaleone, Renormalization of the neutrino mass operator, Phys. Lett. B **319**, 191 (1993).

[81] P. H. Chankowski and Z. Pluciennik, Renormalization group equations for seesaw neutrino masses, Phys. Lett. B **316**, 312 (1993).

[82] W. Grimus and P. Stockinger, Real oscillations of virtual neutrinos, Phys. Rev. D **54**, 3414 (1996).

[83] A. Falkowski, M. González-Alonso, and Z. Tabrizi, Consistent QFT description of non-standard neutrino interactions, J. High Energy Phys. 11 (2020) 048.

[84] C. Giunti, C. W. Kim, J. A. Lee, and U. W. Lee, On the treatment of neutrino oscillations without resort to weak eigenstates, Phys. Rev. D **48**, 4310 (1993).

[85] M. Beuthe, Oscillations of neutrinos and mesons in quantum field theory, Phys. Rep. **375**, 105 (2003).

[86] B. Abi *et al.* (DUNE Collaboration), Deep Underground Neutrino Experiment (DUNE), far detector technical design report, volume II: DUNE physics, arXiv:2002.03005.

[87] C. Andreopoulos, A. Bell, D. Bhattacharya, F. Cavanna, J. Dobson, S. Dytman, H. Gallagher, P. Guzowski, R. Hatcher, P. Kehayias *et al.*, The GENIE neutrino Monte Carlo generator, Nucl. Instrum. Methods Phys. Res., Sect. A **614**, 87 (2010).

[88] C. Andreopoulos, C. Barry, S. Dytman, H. Gallagher, T. Golan, R. Hatcher, G. Perdue, and J. Yarba, The GENIE neutrino Monte Carlo generator: Physics and user manual, arXiv:1510.05494.

[89] A. Friedland and S. W. Li, Understanding the energy resolution of liquid argon neutrino detectors, Phys. Rev. D **99**, 036009 (2019).

[90] Shao-Feng Ge and Kaoru Hagiwara, Physics reach of atmospheric neutrino measurements at PINGU, J. High Energy Phys. 09 (2014) 024.

[91] P. Huber, M. Lindner, and W. Winter, Simulation of long-baseline neutrino oscillation experiments with GLoBES (General Long Baseline Experiment Simulator), Comput. Phys. Commun. **167**, 195 (2005).

[92] P. Huber, J. Kopp, M. Lindner, M. Rolinec, and W. Winter, New features in the simulation of neutrino oscillation experiments with GLoBES 3.0: General long baseline experiment simulator, Comput. Phys. Commun. **177**, 432 (2007).

[93] W. Winter, Neutrino mass hierarchy determination with IceCube-PINGU, Phys. Rev. D **88**, 013013 (2013).

[94] W. Winter, Atmospheric neutrino oscillations for Earth tomography, Nucl. Phys. **B908**, 250 (2016).

[95] B. Abi *et al.* (DUNE Collaboration), Experiment simulation configurations approximating DUNE TDR, arXiv:2103.04797.

[96] M. Antonello *et al.* (ICARUS Collaboration), Search for anomalies in the ν_e appearance from a ν_μ beam, Eur. Phys. J. C **73**, 2599 (2013).

[97] P. Vilain *et al.* (CHARM II Collaboration), Search for muon to electron-neutrino oscillations, Z. Phys. C **64**, 539 (1994).

[98] P. Astier *et al.* (NOMAD Collaboration), Search for $\nu_\mu \to \nu_e$ oscillations in the NOMAD experiment, Phys. Lett. B **570**, 19 (2003).

[99] S. Avvakumov *et al.* (NuTeV Collaboration), A search for $\nu_\mu \to \nu_e$ and $\bar{\nu}_\mu \to \bar{\nu}_e$ oscillations at NuTeV, Phys. Rev. Lett. **89**, 011804 (2002).

[100] M. Gruwe *et al.* (CHARM-II Collaboration), Search for $\nu_\mu \to \nu_\tau$ oscillation, Phys. Lett. B **309**, 463–468 (1993).

[101] P. Astier *et al.* (NOMAD Collaboration), Final NOMAD results on $\nu_\mu \to \nu_\tau$ and $\nu_e \to \nu_\tau$ oscillations including a new search for ν_μ appearance using hadronic τ decays, Nucl. Phys. **B611**, 3 (2001).

[102] D. Naples *et al.* (CCFR/NuTeV Collaboration), A high statistics search for $\nu_e(\nu_e) \to \nu_\tau(\nu_\tau)$ oscillations, Phys. Rev. D **59**, 031101 (1999).

[103] P. Astier *et al.* (NOMAD Collaboration), Prediction of neutrino fluxes in the NOMAD experiment, Nucl. Instrum. Methods Phys. Res., Sect. A **515**, 800 (2003).